A STUDY ON SPARSE ARRAY CONFIGURATIONS FOR ULTRA-WIDEBAND
IMAGING APPLICATIONS

A THESIS SUBMITTED TO
THE GRADUATE SCHOOL OF NATURAL AND APPLIED SCIENCES
OF
MIDDLE EAST TECHNICAL UNIVERSITY

BY

BEYZAT TALAT ÇETİN

IN PARTIAL FULFILLMENT OF THE REQUIREMENTS
FOR
THE DEGREE OF MASTER OF SCIENCE
IN
ELECTRICAL AND ELECTRONICS ENGINEERING

APRIL 2018

Approval of the thesis:

A STUDY ON SPARSE ARRAY CONFIGURATIONS FOR ULTRA-WIDEBAND IMAGING APPLICATIONS

submitted by **BEYZAT TALAT ÇETİN** in partial fulfillment of the requirements for the degree of **Master of Science in Electrical and Electronics Engineering Department, Middle East Technical University** by,

Prof. Dr. Halil Kalıpçılar
Dean, Graduate School of **Natural and Applied Sciences**

Prof. Dr. Tolga Çiloğlu
Head of Department, **Electrical and Electronics Engineering**

Assoc. Prof. Dr. Lale Alatan
Supervisor, **Electrical and Electronics Eng. Dept., METU**

Examining Committee Members:

Prof. Dr. Sencer Koç
Electrical and Electronics Eng. Dept., METU

Assoc. Prof. Dr. Lale Alatan
Electrical and Electronics Eng. Dept., METU

Prof. Dr. Gülbin Dural
Electrical and Electronics Eng. Dept., METU

Prof. Dr. Özlem Aydın Çivi
Electrical and Electronics Eng. Dept., METU

Prof. Dr. Vakur B. Ertürk
Electrical and Electronics Eng. Dept., Bilkent University

Date:

I hereby declare that all information in this document has been obtained and presented in accordance with academic rules and ethical conduct. I also declare that, as required by these rules and conduct, I have fully cited and referenced all material and results that are not original to this work.

Name, Last Name: BEYZAT TALAT ÇETİN

Signature   :

ABSTRACT

A STUDY ON SPARSE ARRAY CONFIGURATIONS FOR ULTRA-WIDEBAND IMAGING APPLICATIONS

Çetin, Beyzat Talat

M.S., Department of Electrical and Electronics Engineering

Supervisor : Assoc. Prof. Dr. Lale Alatan

APRIL 2018, 41 pages

The increased number of terror attacks and crimes have grown a demand for enhancing public security systems. In this sense reliable, cost effective, fast and physically non-hazardous imaging systems should be designed. Multiple-input-multiple-output (MIMO) arrays with ultra-wideband (UWB) technology offers great advantageous for short range imaging applications such as concealed weapon detection (CWD). In this thesis, it is aimed to develop a design tool for MIMO array structures to be used in UWB, near-field (NF) imaging applications. The analyses starts with examination of one-way arrays for better understanding of the nature of UWB arrays. Then, continues with the derivation of point spread function (PSF) for UWB MIMO arrays as a decisive performance parameter. Simulation results of different MIMO array structures that are shared in the literature are examined with derived PSF expression in order to prove the validity of this method. Effects of large operational bandwidth, range to the target and location of the target on observation plane on performance of the array are discussed. Finally, a MIMO array structure to be used in airports for concealed weapon detection is proposed.

Keywords: imaging,MIMO,UWB,near field

ÖZ

GENİŞ BANTLI GÖRÜNTÜLEME SİSTEMLERİNDE KULLANILAN SEYREK ARALIKLI ANTEN DİZİLERİ ÜZERİNE BİR ÇALIŞMA

Çetin, Beyzat Talat

Yüksek Lisans, Elektrik ve Elektronik Mühendisliği Bölümü

Tez Yöneticisi   : Doç. Dr. Lale Alatan

2018 , 41 sayfa

Günümüzde artan suç girişimleri ve terör saldırılar sebebiyle güvenlik sistemlerine duyulan ihtiyaç artmaktadır. Bu sebeple güvenilir, ucuz, hızlı ve sağlık açısından zararı bulunmayan görüntüleme sistemleri tasarlanmalıdır. Çok-Girişli-Çok-Çıkışlı (ÇGÇÇ) anten dizisi yapıları geniş bantlı sinyallerle birlikte bu ihtiyacı karşılama potansiyeline sahiptir. Bu tezde geniş bantlı sinyaller kullanılarak yakın alanda görüntüleme uygulamaları için ÇGÇÇ anten dizilerini tasarlamaya yarayan bir araç geliştirilmesi hedeflenmiştir. Bu amaçla geniş bantlı tek yönlü anten dizileri incelenerek teze başlanmıştır ve sınıflandırma ölçüsü olarak geniş bantlı ÇGÇÇ anten dizileri için Nokta Dağılımı Fonksiyonu (NDF) çıkarımı yapılarak devam edilmiştir. Kullanılan yöntem literatürdeki farklı ÇGÇÇ anten yapılarıyla test edilerek geçerliliği doğrulanmmıştır. Geniş bantlı sinyal kullanmanın etkisi, noktasal hedefin menzilinin ve görüntüleme alanının içerisindeki konumunun etkileri tartışılmıştır. Son olarak geliştirilen tasarım aracıyla havaalanlarında kullanılmak üzere tasarlanacak olan gizlenmiş silah bulma sistemi için bir anten yapısı önerilmiştir.

Anahtar Kelimeler: mikrodalga görüntüleme,yakın alan, geniş bantlı sinyaller

To my dearest family

ACKNOWLEDGMENTS

First of all, I would like to thank my thesis advisor Assoc. Prof. Dr. Lale Alatan for the continuous support throughout my study, for her enthusiasm, remarks and guidance. She continually and convincingly conveyed a spirit of adventure in regard to research. Without her guidance and persistent help none of this would have been possible.

I am also grateful to my parents Ayşe, Asım, my brother Furkan and my life coach, grandmother Şerife for their unlimitted support during my entire life. Thank you for always just wanting the best for me.

Thank you to my friend, Arsen Turhaner. Your infinite belief in me always motivates me. Thank you for always being ready for help and support.

Thank you to my dear wife, Güniz. Thank you for your unconditional love and support since you are in my life.

Thank you to all my friends, for their understanding and support during this thesis.

TABLE OF CONTENTS

LIST OF FIGURES

FIGURES

x

LIST OF ABBREVIATIONS

CW	continous wave
PSF	point spread function
NF	near-field
MIMO	multiple input multiple output
NB	narrow band
UWB	ultra wideband

CHAPTER 1

INTRODUCTION

Imaging systems have been one of the most important and beneficial tools for humankind to explore different properties of materials that are not visible to the naked eye. It is still open to research for developing robust, cost efficient, fast systems. Imaging can be done with different environments like infrared, acoustic waves, neutrons, electromagnetic (EM) fields, etc.

In order to see thruogh visually opaque materials, EM fields in different frequency ranges like gamma ray ($> 3x10^{19}$ Hz), X-Ray ($3x10^{17} - 3x10^{19}$ Hz) and microwave frequencies ($3x10^8 - 3x10^{11}$ Hz) can be used. This property made them useful for medical imaging, security scanning, nondestructive material testing and archeological researches. For example; gamma ray is used in nuclear medical imaging applications such as single-photon emission computed tomography (SPECT) and positron emission tomography (PET) which provide true three dimensional (3-D) information presented as cross-sectional slices [2]. Also, gamma ray detectors are used to scan container cargos shipped to United States (US) in order to increase security as a part of Container Security Initiative (CSI) program [3]. Similarly in medical imaging, X-Ray can be used in computed tomography (CT) scan to construct 3-D images. Also, X-Ray is currently used in most airport security systems. As the wavelength of the light gets shorter, or frequency of EM wave gets higher, energy increases. In the most energetic part of the EM spectrum, there is gamma ray and X-Ray. Because of high energy state gamma ray and X-Ray can ionize atoms, which might be harmful to organisms. Therefore, gamma ray and X-Ray have limited usage on human body. Increased number of terrorist attacks and crimes create a need for concealed weapon detection (CWD) and surveillance systems to be widely used in sensitive security

points. In order to see through optically opaque materials microwave frequencies, between 300 MHz and 300 GHz, can be used without incurring damaging effects. In active microwave imaging systems, the target is illuminated by the microwave transmitter antennas and scattered fields are collected by receiving antennas. Then, received echoes are processed to construct the reflectivity profile of the target. A 3-D system is illustrated in Figure 1.1. to define down-range and cross-range. The image obtained by using narrowband (NB) two-dimensional (2-D) systems have mainly 2-D cross-range information like a photograph, and contain limited information in the down range. By employing ultra-wideband (UWB) signals, it is possible to resolve down-range and obtain 3-D volumetric images. Down-range resolution is determined by signal bandwidth (BW) as in Equation 1.1. where c is speed of light.

$$\delta_{dr} = \frac{c}{2BW} \tag{1.1}$$

Another important parameter for imaging systems is cross-range resolution. Cross-range resolution is related with range, R, wavelength at the center frequency, λ_c, and width of the antenna aperture, L, as given in Equation 1.2.

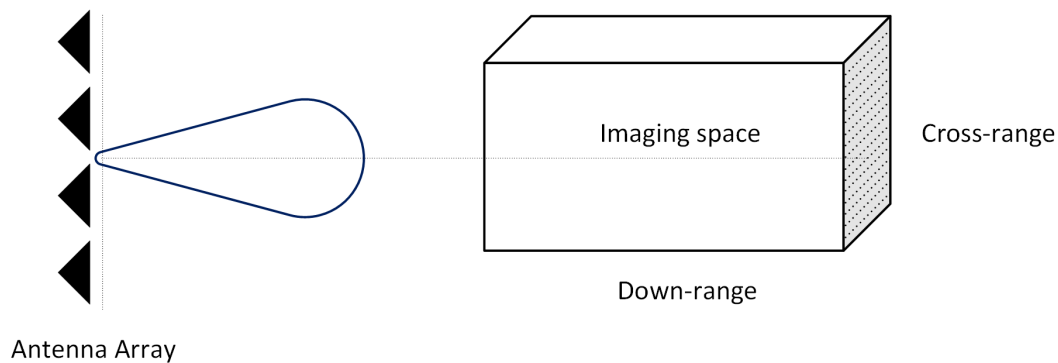$$\delta_{xr} \approx \frac{R\lambda_c}{L} \tag{1.2}$$

Figure 1.1: Illustration of cross-range and down-range.

In conventional NB array theory, inter-element spacing must be close to half-wavelength ($\lambda/2$) in order to prevent grating lobes and sidelobes. For example, in order to achieve

2

1 cm resolution from a target at a range of 1 m, array aperture should be at least 100λ, the elements of the array should be placed in the azimuth and elevation direction which leads to $201x201 = 40401$ elements. Fabrication of such a dense array and design of supporting electronics will be complicated and costly. Also, processing time of the signals retrieved from the object may not be suitable for real time imaging applications.

Therefore the number of elements in the aperture needs to be reduced. Array that has fewer elements required by ($\lambda/2$) element spacing condition is called "sparse arrays". While periodic reduction of array elements results in grating lobes in the radiation pattern, aperiodic array thinning eliminates grating lobes. However in aperiodic arrays, grating lobe energy is distributed over the sidelobes, resulting in higher sidelobe levels. In 1960's many algorithms [4–7] are proposed to design sparse one-way aperiodic arrays. But in [8] Steinberg showed that, most of the algorithms do not give enough control on radiation pattern and array thinning algorithms based on random selection of array elements give similar results. In 1990's it is shown that the high side lobe (or grating lobe) can be eliminated by using UWB signals.

In [9], Schwartz and Steinberg throughly described wideband array behaviour in terms of interception of UWB pulses. Also, there are some additional oppurtunities for grating lobe reduction with multiple-input-multiple-output (MIMO) array method. In [10], Lockwood et al. proposed that in a 1-D MIMO array, sidelobes can be reduced by placing transmitting and receiving antennas with different periodicities. In [11], Lockwood and Foster extended this work for 2-D arrays.

The array aperture for data acquisition can be designed in two different ways. Either there could be a real aperture with N_{tx} number of transmitter and N_{rx} number of receiver elements or a synthetic aperture can be created by moving transmit and receive antennas over the aperture. The later imaging method is Synthetic Aperture Radar (SAR), [12–14]. While SAR is a monostatic approach which contains collocated transmitting and receiving elements, real aperture arrays are generally bistatic configurations especially for MIMO arrays. MIMO arrays offer shorter data acquisition with a cost of increased number of elements. Therefore MIMO-SAR systems are also proposed in the literature [15] that combine advantages of the two systems.

In MIMO-SAR a small real aperture array is scanned over a larger aperture required for the intended resolution. In this way data collection time is reduced compared to SAR system and number of antenna elements are reduced compared to MIMO configuration.

In a typical MIMO imaging system transmit elements illuminates the scene with EM waves and reflected signals from the object are collected by receive array elements. After the received data is processed, image is obtained. Construction of this system can be classified in three design problems: design of MIMO array topology, design of supporting electronics and reconstruction algorithm to obtain image from the received data. This thesis is focuses on the first problem. To design MIMO array, an analysis tool for investigating the performance of different UWB MIMO array configurations is required. The aim of this thesis is to develop such an analysis tool that is not based on any one of the image reconstruction algorithms and also provides results with an accuracy close to the accuracy that can be obtained from full-wave simulation softwares. To achieve this, first the method proposed in [9] is implemented and it is improved by incorporating the radiation patterns of the array elements into the formulation.

Thesis starts with the review of existing theories developed for the of UWB arrays in Chapter 2. In Chapter 3 derivation of Point Spread Function (PSF) for a MIMO array operating in UWB will be presented by considering a point scatterer. The performance of different array configurations will be compared by using the PSF results obtained from the developed code. Some of the results have already been given in [16] and further study given in this thesis. After the developed code obtained results in good agreement with the experimental and simulation results in [1], the code is extended to include the effects of antenna radiation patterns into the PSF calculations. The formulations related to this extension are presented in this chapter. Moreover the simulation results obtained for different MIMO-SAR configurations are also presented in this chapter and conclusions are drawn in Chapter 4.

CHAPTER 2

ANALYSIS OF ULTRA-WIDEBAND ANTENNA ARRAYS

The conventional analysis of antenna arrays is generally based on NB single frequency assumption, which is also referred to as "monochromatic" analysis. Under this assumption, it is sufficient to consider only the steady state behaviour in the analysis. However; when an UWB pulse excitation as shown in Fig. 2.1 is considered, due to the short duration and fast variation of the pulse, transient behaviour also becomes important. Hence the analysis needs to be performed in the time domain. This time domain analysis results in some significant differences between the analysis of arrays operating in NB and UWB.
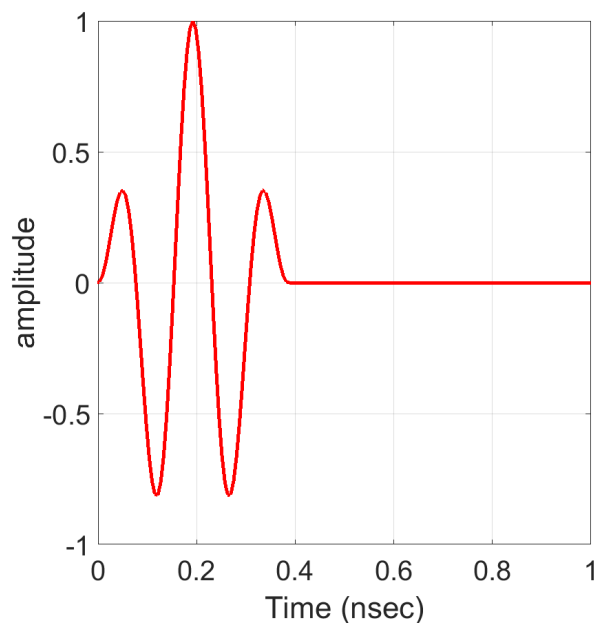
Figure 2.1: UWB Pulse

First of all, the far-field radiation pattern of a NB array is a function of only the

azimuth and elevation angles. However, the far-field radiation pattern of a UWB array depends on both the azimuth and elevation angles and also the time instance. Therefore, the radiation pattern is generally referred as "radiation function" for UWB case due to this time dependence.

Secondly, since the NB signal is sinusoidal for all time instances, the radiated fields from two seperate antennas interfere for all time instances and observation angles whereas UWB pulses transmitted from two separate antennas interfere only for some range of observation angles determined by the duration of the pulse and the separation of the antenna. Therefore it is possible to define an "Interference Region (IR)" and "Non-interference Region (NIR)" for UWB case. Consequently, by choosing the element spacings properly, it is possible to eliminate the grating lobes in UWB arrays, by pushing them into the NIR. In this chapter, side lobes performance of NB and UWB arrays will be discussed by comparing numerical results obtained for similar arrays. The numerical analysis starts by the derivation of the radiation function for a planar periodic array as shown in Fig. 2.2, $\bar{r}_i'$ denotes the location of the i_{th} element, $\bar{r}$ denotes observation point, $w(\bar{r}_i)$ denotes the weight (amplitude) of the element at $\bar{r}_i'$. The radiation function $R(\bar{r}, t)$ can be written as follows by assuming an UWB pulse radiation denoted by p(t):
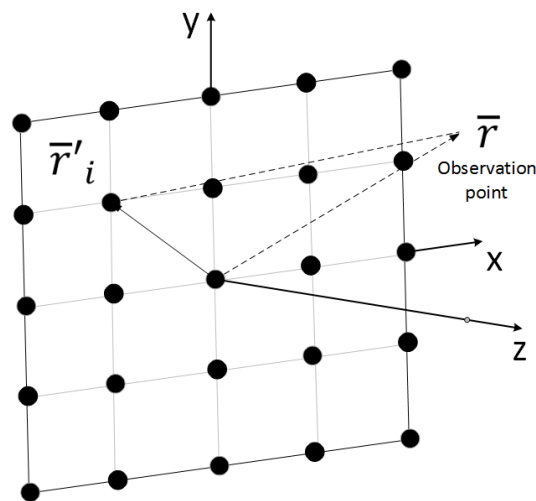

Figure 2.2: Planar periodic array

$$R(\bar{r}, t) = \sum_{i=1}^{N} w(\bar{r}_i') \frac{p\left(t - \left|\frac{\bar{r}-\bar{r}_i'}{c}\right|\right)}{\left|\frac{\bar{r}-\bar{r}_i'}{c}\right|} \tag{2.1}$$

where c is the speed of light. If the medium is different than free space, c should be replaced by the phase velocity in that medium. Equation 2.1. is a general expression valid for both near-field (NF) and far-field. When far-field is considered, $|\bar{r} - \bar{r}_i'|$ in the time delay and in the denominator can be approximated as;

$$Time\ delay : |\bar{r} - \bar{r}_i'| = r - x_i u - y_i v$$
$$Denominator : |\bar{r} - \bar{r}_i'| = r \tag{2.2}$$

where,

$$u = \sin\theta\cos\phi$$
$$v = \sin\theta\sin\phi \tag{2.3}$$

Hence Equation 2.1. simplifies to the following;

$$R(\bar{r}, t) = \frac{1}{r} \sum_{i=1}^{N} w(\bar{r}_i') p\left(t' + \frac{x_i u}{c} + \frac{y_i v}{c}\right) \tag{2.4}$$

where t' is defined as the incremental time that starts at the instant the UWB pulse reaches the observation point r/c. The far-field radiation function of a 10 element linear array placed along x-axis with an element spacing $2\lambda_c$ wavelength at center frequency, f_c, is obtained by assuming the following UWB pulse with 2.6 GHz bandwidth (BW) at 6.5 GHz center frequency,

$$p(t) = \sin(2\pi f_c t)\cos\left(\frac{\pi t}{BW}\right) rect_{BW}(t) \tag{2.5}$$

where $rect_{BW}$ denotes a rectangular pulse with length $1/BW$. The 2-D radiation function is presented in Fig. 2.3 together with two angular cuts at $\theta = 0°$ and $\theta = 90°$
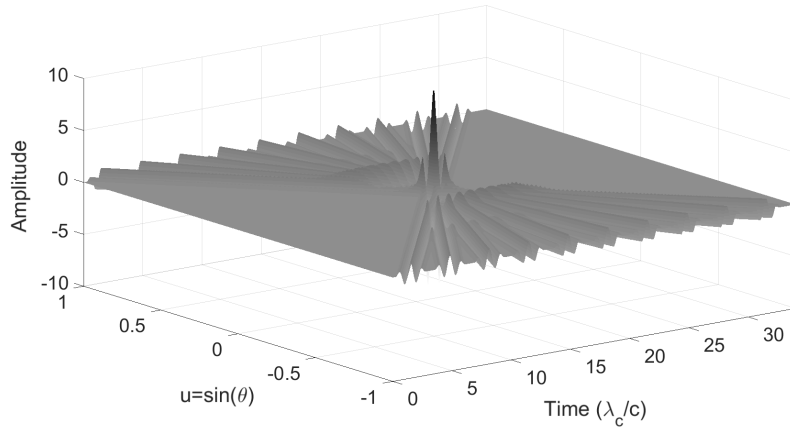
(a)
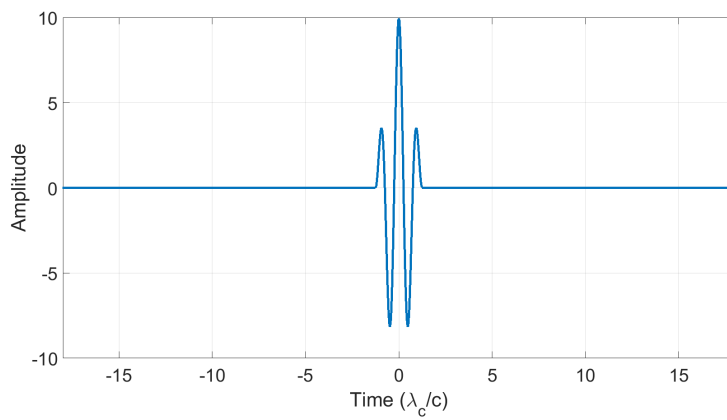
(b)
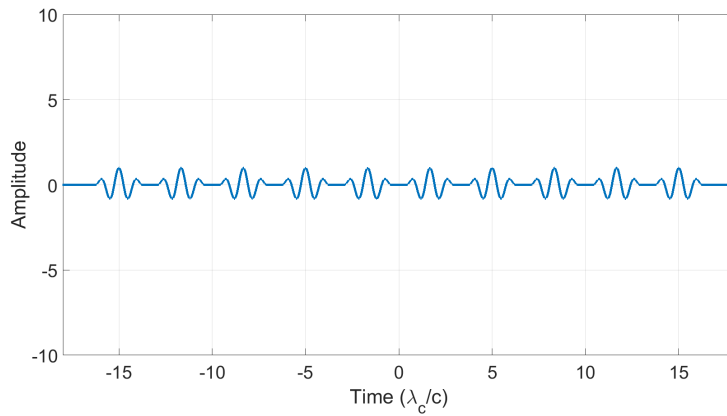
(c)

Figure 2.3: Radiation pattern of a 10 element UWB array with $2\lambda_c$ spacings (a) 2-D radiational pattern (b) $\theta = 0°$ angular cut, (c) $\theta = 90°$ angular cut

In order to compare the performance of NB and UWB arrays for the same number of array elements and inter-element spacings, the time dependence in radiation func-

tion of the UWB array needs to be eliminated. For this purpose different approaches are proposed in the literature. For example, integrating the radiation function with respect to time to end up with energy is proposed in [17]. The energy pattern and the fidelity parameters defined in [17] found widespread application in evaluating the performance of UWB antennas used in communication systems in [18–20]. However when the performance of antenna arrays used in imaging systems are concerned, the peak side energy levels are more important than the integral sum of all values with respect to time. Therefore maximum projection method is proposed in [21]. In this method, for a given observation angle, the maximum value of the radiation function over all time instances is choosen. Consequently, the maximum envelope of the radiation function onto the angle axis gives the radiation pattern as shown in Fig. 2.4.
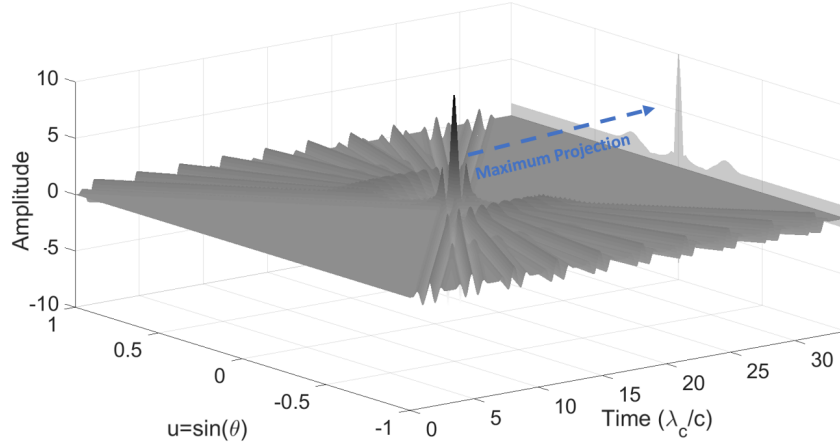
Figure 2.4: Illustration of maximum projection on radiation function.

The radiation pattern of 3 different linear arrays with same array length ($18\lambda_c$) are compared in Fig. 2.5 for NB and UWB cases. For UWB case, first radiation function is obtained by using the 40% BW pulse defined in Equation 2.5. Then, the radiation pattern is obtained by using maximum projection theorem. Array 1 is a 37 element array with $\lambda_c/2$ spacing. Array 2 is a 10 element array with $2\lambda_c$ spacing. Array 3 is a randomly distributed 10 element array with an average spacing of $2\lambda_c$, where λ_c is the wavelength at 6.5 GHz center frequency.

When the results of NB array are investigated, it can be observed that grating lobes occur for periodic array with $2\lambda_c$ and when the periodicity is disturbed, grating lobes
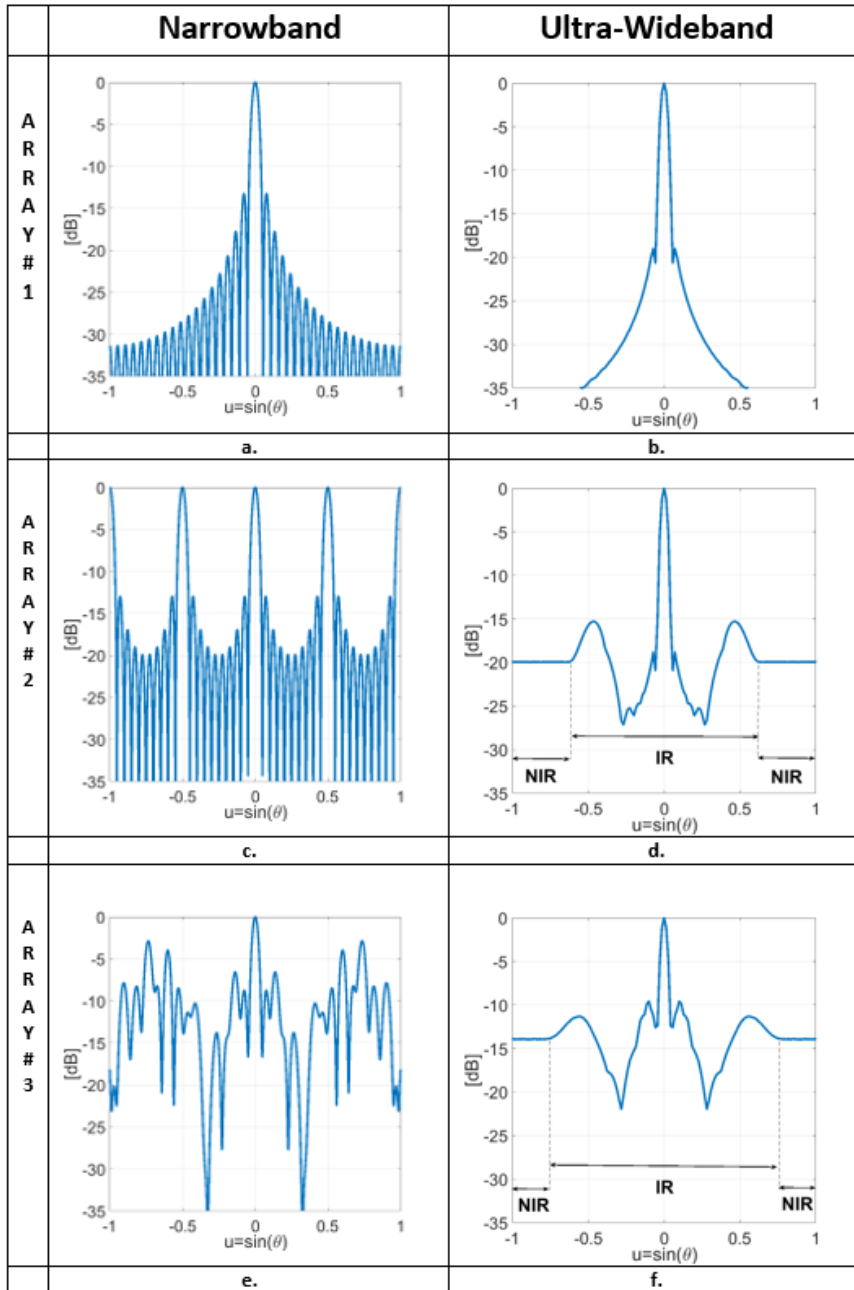
Figure 2.5: NB and UWB radiation pattern comparisons of 37 elements linear (a,b), 10 elements linear (c,d), 10 elements random (e,f) arrays.

are eliminated but the overall sidelobe levels are increased as expected. However, the results of UWB array are quite interesting. First of all, the sidelobe level of the periodic array for $2\lambda_c$ spacing is around -14 dB, which is very low compared to the NB array where grating lobes occur. As discussed before, this is due to the fact that all the array elements add up coherently for the NB array but for the UWB array,

the transmitted pulses will interfere only if the propagation delay time between two elements is less than the duration of the pulse,T. This can be better understood by examining Fig. 2.6., where the interference of two elements seperated by a distance d is illustrated.
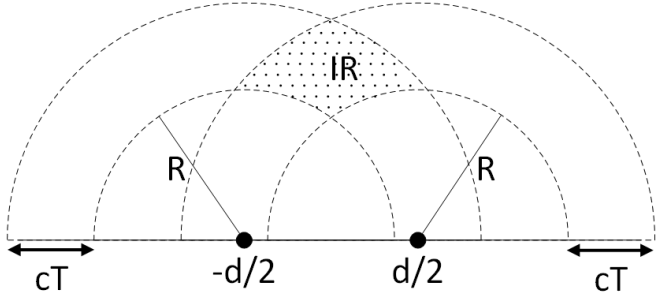
Figure 2.6: Illustration of maximum projection on radiation function.

The radius of the inner half circles are the observation distance, R. The radiated pulses start there. The radius of the outer half circles are R+cT that represents the end of the pulse. Two pulses transmitted from the antennas will exist simultaneously only in the shaded area denoted by IR. It can be seen that, IR will be smaller if d is longer, T is shorter and target is closer (smaller R). This discussion also explains the reason why the randomly distributed array results in a higher sidelobe level for UWB case. For a fixed aperture size and a fixed number of elements, maximum element spacing could be achieved only with periodic array. For a randomly distributed array some of the element spacings will be smaller than this periodic spacing and those close elements will interfere resulting in a higher sidelobe level. The first important conclusion of this study states that the best performance in terms of sidelobe level, for a UWB array can be obtained by periodic placement. Secondly, the side energy level of the plateu in the NIR is determined by the number of noninterfering elements. For periodic array neither of the elements interfere in NIR and we observe seperate pulses as shown in Fig. 2.3c. But in the main beam direction all pulses add up coherently and the magnitude becomes N times the amplitude of the pulse. Consequently, the ratio of the power level at the plateu to the peak power is 20log(1/N). This ratio is called as ideal sidelobe level (ISL). For 10 element array ISL is -20 dB which is consistent with the numerical result. Hence the second important conclusion is that ISL can be reduced by increasing the number of array elements.

The discussions carried out so far were limited to one dimensional linear arrays. However for two dimensional imaging, a planar array is required. The analysis of UWB planar arrays are generally performed by using projection slice method [22]. In projection slice method, radiation pattern of a 2-D array in an angular cut is calculated from radiation pattern of 1-D array which is the projection of the elements on that particular angular cut. An example of projection slice method can be seen in Fig. 2.7.
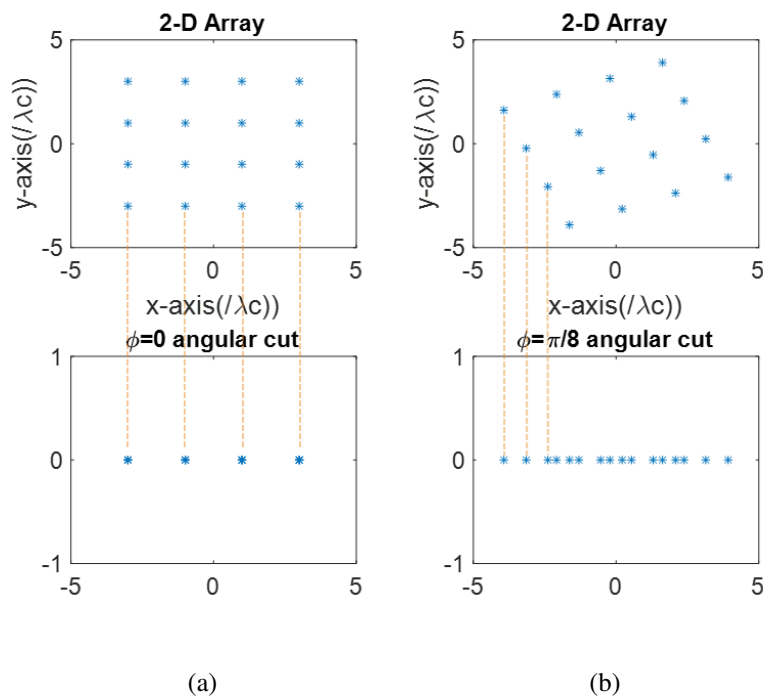
Figure 2.7: 2-D periodic rectangular array at different azimuth cuts corresponding radiation patterns in that angular cut. (a) Appearance of the array at $\phi = 0$ and angular cut (b) Appearance of the array at $\phi = \pi/8$ and angular cut

In Fig. 2.7a. the radiation pattern of all array elements on $\phi = 0$ axis are plotted, all elements with same x location will appear at the same position. Hence the projected linear array will have only 4 elements. However when the radiation pattern at $\phi = \pi/8$ is considered as in Fig. 2.7b., all 16 elements will appear at separate locations in the projected array. Since it was concluded that ISL decreases with N in a linear array, a much better sidelobe performance is expected for $\phi = \pi/8$. The radiation patterns at $\phi = \pi/8$ and $\phi = 0$ are compared in Fig. 2.8. As expected the sidelobe level is 12-13 dB lower at $\phi = \pi/8$ cut. At $\phi = 0$ since a periodic 4 element array

12

occurs, $ISL = 20log(\frac{1}{4}) = -12dB$ is expected and observed. ISL of a periodic 16 element array is -20log16=-24dB. For $\phi = \pi/8$ a slightly higher ISL is observed and side plateau does not occur due to the aperiodic nature of the projected array. When periodic configurations are used for 2-D arrays, high sidelobe levels are expected at the two principal axis of the array. Since all elements along a line appears as a single element when projected onto the axis which is perpendicular to this line, this concept is named as shadowing.
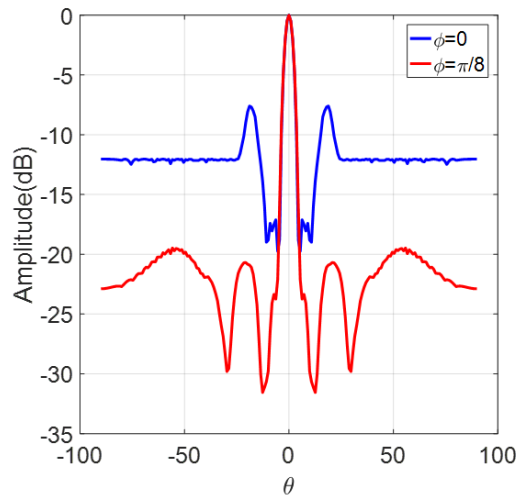
Figure 2.8: Radiation pattern comparison at $\phi = 0$ and $\phi = \pi/8$.

To avoid shadowing concentric rings, spiral and circular configurations as shown in Fig.2.9 are proposed in the literature.
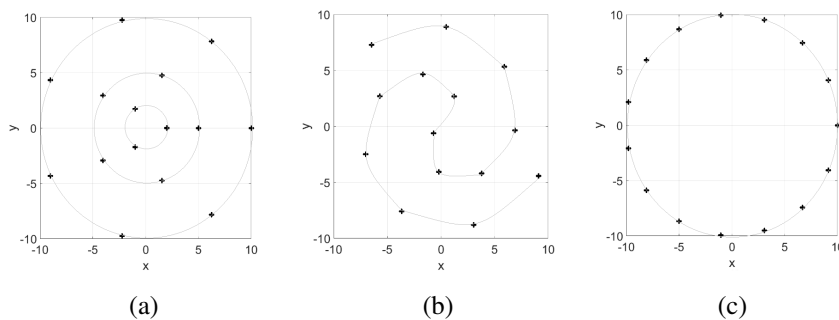
Figure 2.9: 2-D array structures to avoid shadowing. (a) multiple-ring (b) spiral (c) circular structure.

The analysis presented in this chapter consider only one way radiation from the array. However the scope of this thesis is imaging systems working with MIMO arrays.

Therefore, in the next chapter analysis will be extended to obtain two-way radiation patterns that include both the transmit and the receive arrays.

CHAPTER 3

MULTIPLE INPUT MULTIPLE OUTPUT ARRAYS

Point spread function (PSF) is a figure of merit to define the quality of an imaging system. To obtain PSF, a point scatterer with reflectivity 1 is considered at location $\bar{r}_0$. PSF corresponds to the image formed due to this point scatterer. Figure 3.1. illustrates a MIMO array with N_{rx} number of receive elements and N_{tx} number of transmit elements. Receiving and transmitting element locations are $\bar{r}_{rx}$ and $\bar{r}_{tx}$, respectively. Each element in the receive and transmit arrays is assumed to have a weighting coefficient w_{rx} and w_{tx}, respectively. The field transmitted from the element at $\bar{r}_{tx}$ will arrive to point scatterer at $t = | \bar{r}_{tx} - \bar{r}_0 | / c$. The field reflected by the scatterer is received by receiving element, $\bar{r}_{tx}$, at $t = (| \bar{r}_{rx} - \bar{r}_0 | + | \bar{r}_{tx} - \bar{r}_0 |)/c$. Then the Green's function for a two-way MIMO array becomes,

Figure 3.1: 2-D MIMO Array.

$$G(\bar{r}_0, \bar{r}_{tx}, \bar{r}_{rx}, t) = \frac{\delta\left(t - \frac{|\bar{r}_0 - \bar{r}_{tx}|}{c}\right)}{4\pi|\bar{r}_0 - \bar{r}_{tx}|} * \frac{\delta\left(t - \frac{|\bar{r}_{rx} - \bar{r}_0|}{c}\right)}{4\pi|\bar{r}_{rx} - \bar{r}_0|}$$
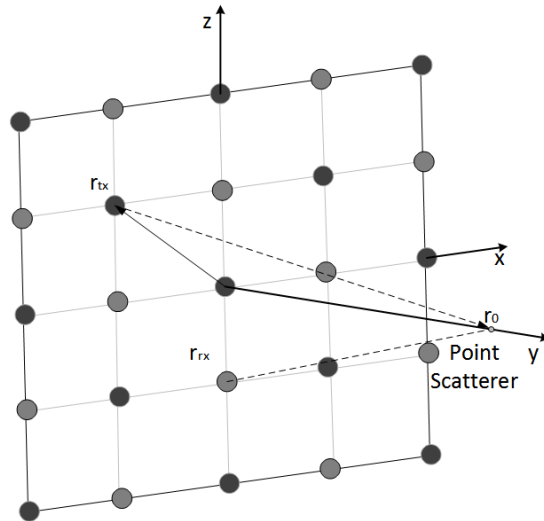
$$= \frac{\delta\left(t - \frac{(|\bar{r}_0 - \bar{r}_{tx}| + |\bar{r}_{rx} - \bar{r}_0|)}{c}\right)}{16\pi^2|\bar{r}_0 - \bar{r}_{tx}||\bar{r}_{rx} - \bar{r}_0|} \tag{3.1}$$

where * denotes convolution operation. The signal received for each transmit-receive pair for a transmitted pulse $p(t)$, can be written as:

$$u(\bar{r}_0, \bar{r}_{tx}, \bar{r}_{rx}, t) = w_{tx}(\bar{r}_{tx})w_{rx}(\bar{r}_{rx})G(\bar{r}_0, \bar{r}_{tx}, \bar{r}_{rx}, t) * p(t)$$

$$= w_{tx}(\bar{r}_{tx})w_{rx}(\bar{r}_{rx})\frac{p\left(t - \frac{(|\bar{r}_0 - \bar{r}_{tx}| + |\bar{r}_{rx} - \bar{r}_0|)}{c}\right)}{16\pi^2|\bar{r}_0 - \bar{r}_{tx}||\bar{r}_{rx} - \bar{r}_0|} \tag{3.2}$$

By using these received signals, utilizing different methods proposed in literature [23–25] the image of the object can be constructed. In this thesis the approach used in [1] is used. This approach is based on focused radar principle such that when point r in image space is considered, both the transmit and receive arrays are excited with corresponding time delays so that their beams are focused at r. Corresponding time delays can be expressed in the following form:

$$\Gamma(\bar{r}, \bar{r}_{rx}, \bar{r}_{tx}, t(\bar{r}_{rx})) = \frac{(|\bar{r} - \bar{r}_{tx}| + |\bar{r}_{rx} - \bar{r}|)}{c} \tag{3.3}$$

The image of the object can be obtained by scanning the focus point throughout the image space as:

$$PSF(\bar{r}_0, \bar{r}, t) = \int_{\bar{r}_{tx}} \int_{\bar{r}_{rx}} u(\bar{r}_0, \bar{r}_{rx}, \bar{r}_{tx}, \Gamma(barr, \bar{r}_{rx}, \bar{r}_{tx}, t(\bar{r}_{rx})))dr_{rx}dr_{tx}$$

$$= p(t) * \int_{\bar{r}_{tx}} w_{tx}(\bar{r}_{tx})\frac{\delta(t - T_{tx}(\bar{r}, \bar{r}_{tx}))}{4\pi|\bar{r}_0 - \bar{r}_{tx}|}dr_{tx}$$

$$* \int_{\bar{r}_{rx}} w_{rx}(\bar{r}_{rx})\frac{\delta(t - T_{rx}(r, \bar{r}_{rx}))}{4\pi|\bar{r}_0 - \bar{r}_{rx}|}dr_{rx} \tag{3.4}$$

$$= \int_{\bar{r}_{tx}} \int_{\bar{r}_{rx}} \frac{p(t - T_{tx}(r, \bar{r}_{tx}) - T_{rx}(r, \bar{r}_{rx}))}{16\pi^2|\bar{r}_0 - \bar{r}_{tx}||\bar{r}_0 - \bar{r}_{rx}|}w_{tx}(\bar{r}_{tx})w_{rx}(\bar{r}_{rx})dr_{rx}dr_{tx}$$

16

where receive, T_{rx}, and transmit, T_{tx}, relative delays are:

$$T_{tx}(\bar{r}, \bar{r}_{tx}) = (|\ \bar{r}_0 - \bar{r}_{tx}\ | - |\ \bar{r} - \bar{r}_{tx}\ |)/c$$

$$T_{rx}(\bar{r}, \bar{r}_{rx}) = (|\ \bar{r}_{rx} - \bar{r}_0\ | - |\ \bar{r}_{rx} - \bar{r}\ |)/c$$

$$(3.5)$$

In the next section, the performance of 3 different MIMO array configurations will be compared based on their PSF results. However before proceeding to the simulation results, it is worth discussing an important concept which is virtual array or effective aperture concept.

3.1 Effective Aperture

Effective aperture is a useful tool to investigate MIMO arrays, because it is a mathematical equivalance to reduce a two-way receive transmit array to a one way array. The usability of this method in far-field is explained in [9] and it is further proved in [1] that it can be used in nearfield wideband applications. Basically, each transmit-receive pair is replaced by an equivalent virtual element. The location $\bar{r}_{Emn}$ and weighting coefficient w_{Emn} of the mn^{th} virtual element can be written as:

$$\bar{r}_{Emn} = \bar{r}_{Tm} + \bar{r}_{Rn}$$

$$w_{Emn} = w_{Tm}.w_{Rn}$$

$$(3.6)$$

where $\bar{r}_{Rn}$ and $\bar{r}_{Tm}$ are locations of transmitting and receiving element, respectively. Similarly, weighting coefficients of transmitting and receiving elements are w_{Tm} and w_{Rn}, respectively. The array formed by all virtual elements is called "virtual array" or "effective aperture".

In Fig. 3.2, effective aperture of three different MIMO array configurations with same number of total $N_{rx} + N_{tx}$ array elements are presented. When two elements in the effective aperture are overlapping or they are very close to each other one of the these elements can be considered as redundant since they provide same information. This is called redundancy and to avoid it uniform distribution of elements is prefered.

17
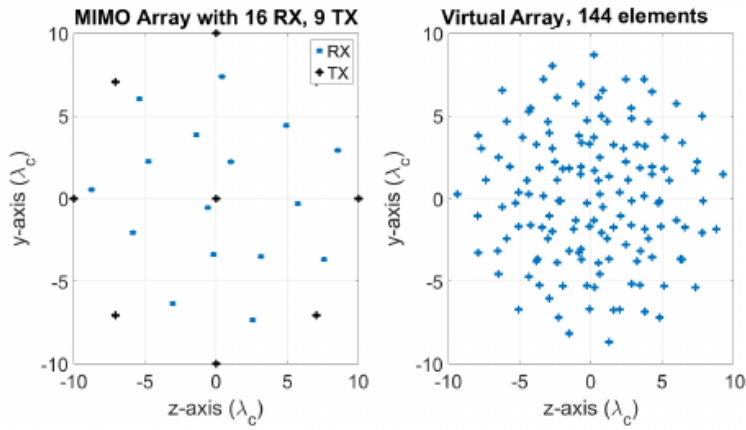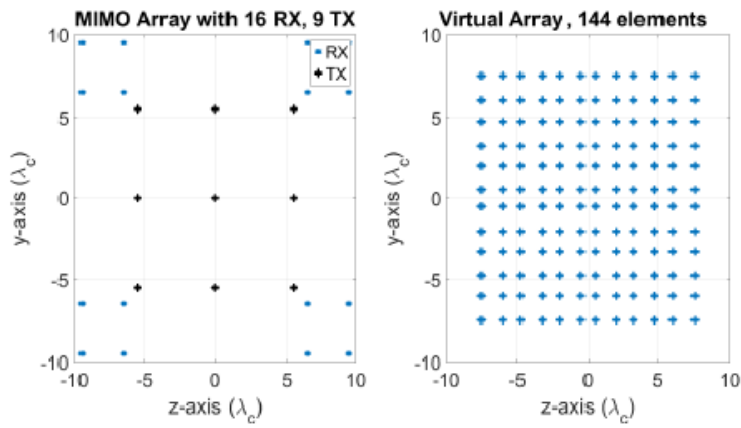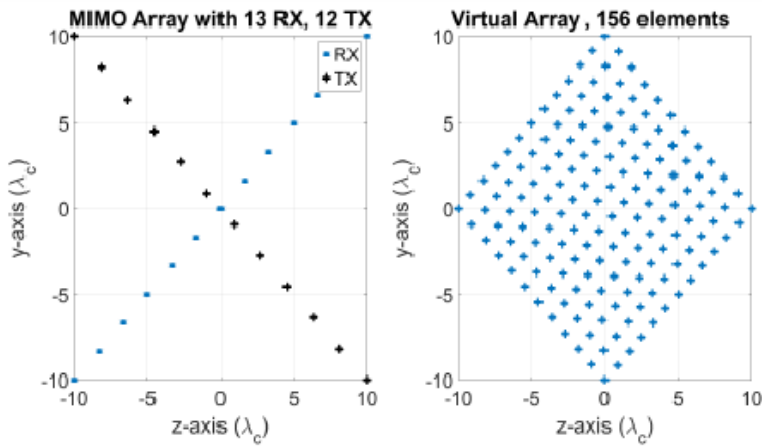
Figure 3.2: Array configurations. (a) Curvilinear array (b) Rectangular array (c) Mill's cross array

From Fig. 3.2 it can be observed that Mill's cross and rectangular arrays provide more uniform distribution than curvilinear arrays due to the periodic placement of the MIMO array elements. However as discussed in Chapter 2 periodic arrays suffer from shadowing problem that results in increased side lobe levels along directions perpendicular to the periodicity. Therefore the compromise between redundancy and shadowing should be considered simultaneously during the design of MIMO arrays.

3.2 Simulation Results

In order to compare the performance of three different MIMO array configurations presented in Fig. 3.2, their PSF's are computed by using the formulation presented in the previous section. The computed PSF results will be compared with the simulation results presented in [26]. In [26] the signals received by each transmit-receive pair for a scatterer are computed by using a full-wave electromagnetic simulator FEKO. During simulations antennas are modelled as Hertzian dipoles. Then these signals are used as input to the image reconstruction algorithm which is chosen as modified Kirchhoff migration [23] method in [26]. It should be noted that the analyses in FEKO are carried out in frequency domain. Hence before feeding this information to modified Kirchhoff migration method which is a time domain algorithm, inverse Fourier Transform of the received signals are calculated. Hence, since a rectangular pulse is assumed in frequency domain, the shape of the time domain pulse turns out to be a sinc function. However finite duration time domain pulse is assumed for the formulation presented in this chapter. After comparing different pulse shapes proposed in the literature the generalized Gaussian pulse (GGP) used in [1] is chosen for the analyses presented in this thesis. The mathematical representation of the GGP is as follows:

$$p(t) = E_0 \sum_{k=0}^{1} I_k exp\left(- a_k[(t - t_0)/\Delta T]^2\right) \tag{3.7}$$

where ΔT is nominal duration, I_k and a_k coefficients are,

19

$$I_k = 1/(1 - \alpha), I_1 = -\alpha(1 - \alpha), \alpha \neq 1 \qquad (3.8)$$

$$a_0 = 4\pi, a_1 = 4\pi\alpha^2 \qquad (3.9)$$

The shape of the pulse can be tuned by the scaling parameter α and E_0 is the peak voltage of $p(t)$ at $t = t_0$. The shape of the pulse for $\alpha = 0.6$ $E_0 = 1$ and $t_0 = \Delta T \approx 0.15nsec$ is presented in Fig. 3.3.
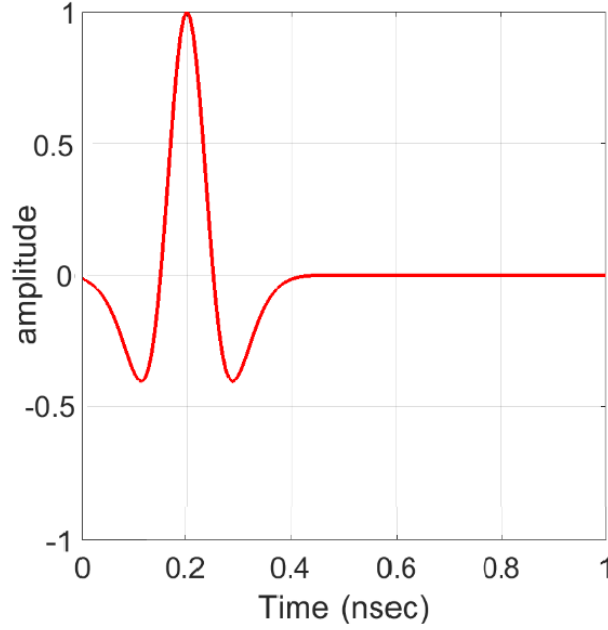
Figure 3.3: Time domain UWB pulse shape used in this chapter.

In the cross range, a point scatterer is placed at the center of the array aperture. The PSF results are obtained for 4 different positions of the scatterer in the down range ($20\lambda_c, 30\lambda_c, 40\lambda_c, 60\lambda_c$). The parameters of the GGP pulse are chosen as for $\alpha = 0.6$ $E_0 = 1$ and $t_0 = \Delta T \approx 0.15nsec$. The calculated PSF results along x-axis for three different array configurations are presented in the left column of Fig. 3.4 for 4 different range values. The results presented in [26] for the same array configurations and %150 bandwidth are also presented in the right column of Fig. 3.4. As discussed before due to the differences in modeling the time domain pulse it is not possible to make a fair comparison. Still the results presented in [26] are included in the figure to check the validity of the approach presented in this chapter.

Figure 3.4: Comparison of the calculated PSF results (on the left column) with the results presented in [1] (on the right column). PSF's of (a-b) Curvilinear, (c-d) rectangular,(e-f) Mill's cross aray topologies .

When the PSF calculation results of three different MIMO array topologies given in Fig. 3.2 with equal number of elements are compared, the best side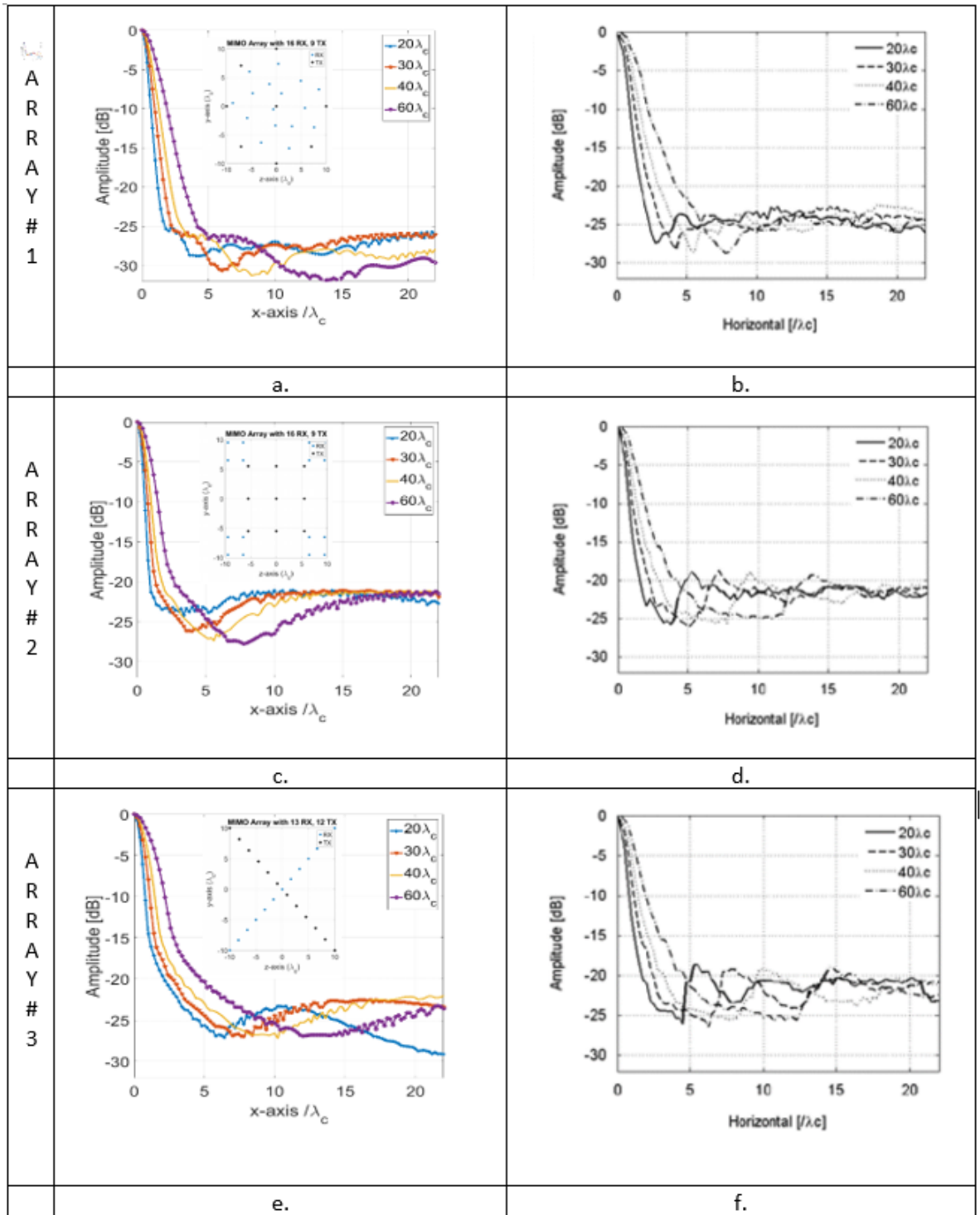lobe performance is observed for curvilinear MIMO array structure in Fig. 3.4.a. The reason laying behind this performance is aperiodic receive and transmit array structure that result in random like distribution of virtual array. Therefore, less shadowing exist with curvilinear structure when compared with periodic Mill's cross and rectangular structures. As previously mentioned periodical structures suffer from sidelobe degradation in the axes where shadowing occurs.

Comparing the calculated PSF's in Fig. 3.4.a,c,e. with the PSF's given in the reference work in Fig. 3.4.b,d,f. the sidelobe characteristics is not fully compatible but the best array topology is discriminated in both ways. Therefore time domain method used here can be applied as a performance comparison tool. But, as previously mentioned, method applied in [26] gathers the data about the imaging space in frequency domain. In order to obtain more fair comparison with this reference work, the calculations will be carried out in frequency domain in the following section.

3.3   Point Spread Function in Frequency Domain

In this section PSF will be calculated by using a frequency domain pulse. The pulse used here is simply a uniform rectangular pulse shape which covers operational bandwidth. Sampling frequency is 10 MHz throughout the analyses. Recall the PSF expression previously given,

$$PSF(\bar{r}_0, \bar{r}, t) = \int_{\bar{r}_{tx}} \int_{\bar{r}_{rx}} \frac{p(t - T_{tx}(\bar{r}, \bar{r}_{tx}) - T_{rx}(\bar{r}, \bar{r}_{rx}))}{16\pi^2 \mid \bar{r}_0 - \bar{r}_{tx} \parallel \bar{r}_0 - \bar{r}_{rx} \mid} w_{tx}(\bar{r}_{tx}) w_{rx}(\bar{r}_{rx}) dr_{rx} dr_{tx} \quad (3.10)$$

Before using equation 3.10, frequency domain pulse need to be converted into the equivalent time domain form by applying Inverse Fourier Transform. Let, $p(t)$ be the exciting pulse shape and $P(f)$ be the Fourier transform of the pulse shape. The Fourier transform relation between them is as follows,

$$p(t) = \frac{1}{2\pi} \int_{-\infty}^{\infty} P(f)e^{j2\pi ft} df \quad (3.11)$$

22

Time delays in equation 3.10, $T_{rx}(\bar{r}, \bar{r}_{rx})$ and $T_{rx}(\bar{r}, \bar{r}_{rx})$, to scan the imaging space corresponds to phase shift, in frequency domain. Phase shifted pulse must be converted into time domain before applying equation 3.10. Phase shifted pulse can be calculated as follows,

$$p(t - T_{tx}(\bar{r}, \bar{r}_{tx}) - T_{rx}(r, \bar{r}_{rx})) = \frac{1}{2\pi} \int_{-\infty}^{\infty} P(f)e^{-j2\pi f(T_{tx}(\bar{r}, \bar{r}_{tx}) + T_{rx}(\bar{r}, \bar{r}_{rx}))} e^{j2\pi ft} df \quad (3.12)$$

where receive, T_{rx}, and transmit, T_{tx}, relative delays are:

$$T_{tx}(\bar{r}, \bar{r}_{tx}) = (\mid \bar{r}_0 - \bar{r}_{tx} \mid - \mid \bar{r} - \bar{r}_{tx} \mid)/c$$
$$T_{rx}(\bar{r}, \bar{r}_{rx}) = (\mid \bar{r}_{rx} - \bar{r}_0 \mid - \mid \bar{r}_{rx} - \bar{r} \mid)/c \quad (3.13)$$

MIMO array structures given in Fig. 3.2 is examined with the implementation of formulations given in equations 3.10 and 3.12. In the calculations %150 bandwidth with center frequency at 6.5 GHz is assumed. The results of the calculated PSF's are given in Fig. 3.5 together with the results obtained in the reference work [26].

In Fig. 3.5 again curvilinear structure gives the best results in terms of sidelobe in Fig. 3.5.a. and Fig. 3.5.b because it contains less shadowing in virtual array. Also, curvilinear structure is immune to degradation of the sidelobes as the range to the point target gets shorter. Although, calculations made with time domain pulse in Fig.3.4. was proper to compare the performances of different MIMO array structures, the shape of the sidelobes was not close to the reference work. These results show that sidelobe characteristics of the calculated PSF's better match with the reference work when compared with the calculations carried with time domain pulse. Even a better agreement is observed, there are some differences between the results obtained in this work and in [26]. It should be noted that in [26] full-wave simulation results are used in modified Kirchoff Migration method but in this work focused radar approach is used with maximum projection method. These different approaches give rise to the differences in the results

The reference work [26] Hertzian dipoles employed in the full-wave simulations. But in real life, antenna elements are not isotropic like Hertzian dipoles. Hence, it may
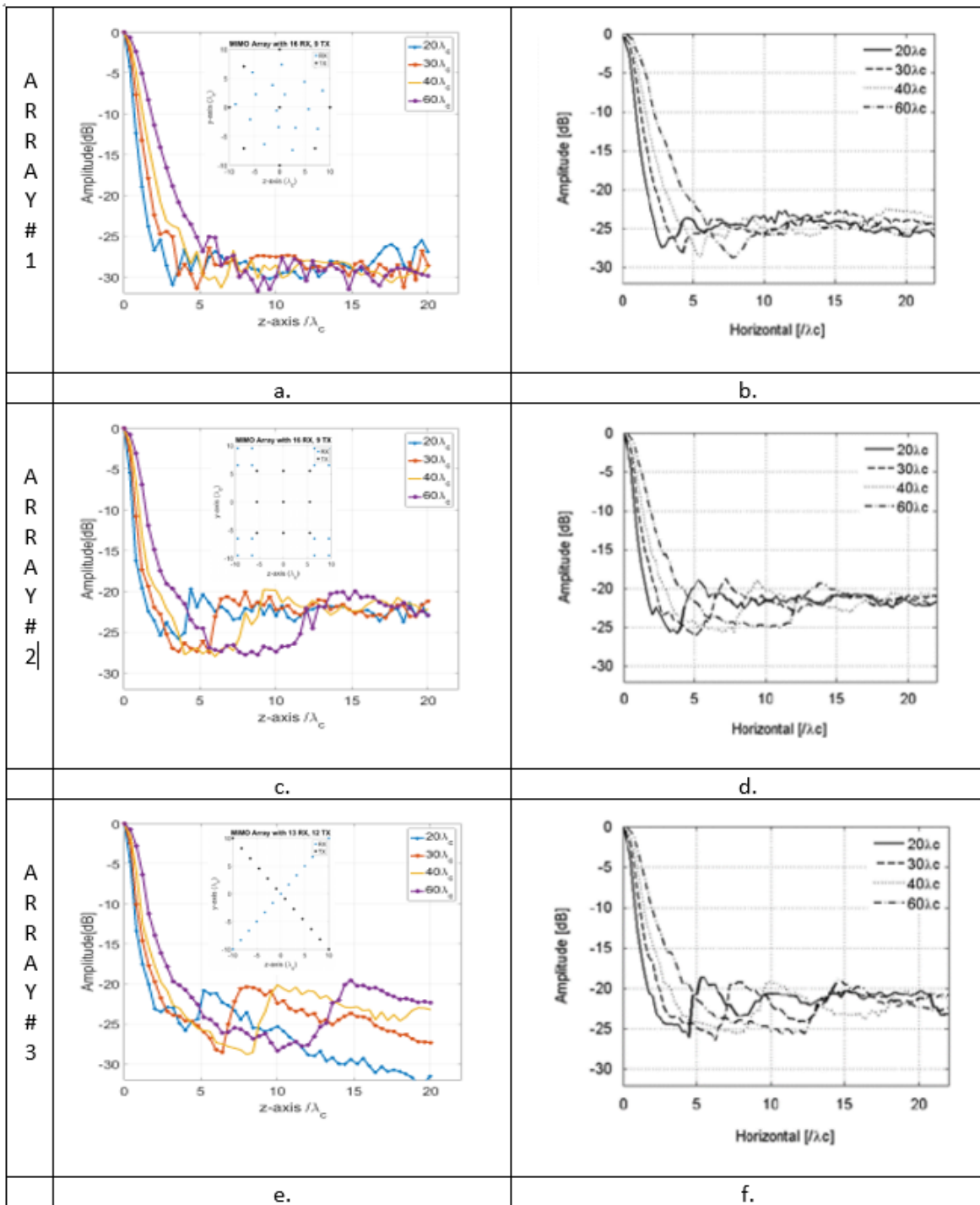
Figure 3.5: Comparison of the calculated PSF results (on the left column) with the results presented in [1] (on the right column). PSF's of (a-b) Curvilinear, (c-d) rectangular,(e-f) Mill's cross aray topologies .

not be possible to obtain information from far array elements in the antenna aperture. In order to model real life situations, element patterns of the array elements need to be taken into account. The element pattern data retrieved from measurement or simulation of an antenna element is in frequency domain. Therefore, it can be implemented as a multiplier for the exciation pulse corresponding to each receive-transmit antenna pair as in equation 3.14,

$$p(t - T_{tx}(\bar{r}, \bar{r}_{tx}) - T_{rx}(r, \bar{r}_{rx})) =$$
$$\frac{1}{2\pi} \int_{-\infty}^{\infty} P(f)e^{-j2\pi f(T_{tx}(\bar{r}, \bar{r}_{tx}) + T_{rx}(r, \bar{r}_{rx}))} F_{rx}(\theta_r, f) F_{tx}(\theta_t, f) e^{j2\pi ft} df$$

$$(3.14)$$

where $F_{rx}(\theta_r, f)$ and $F_{tx}(\theta_t, f)$ are relative element patterns of receive and transmit elements corresponding to the θ_r and θ_t angles that receive/transmit elements made with the scatterer. Element pattern multipliers for each recieve-transmit antenna pair are found as illustrated in Figure 3.6 by simple geometry.

(a)
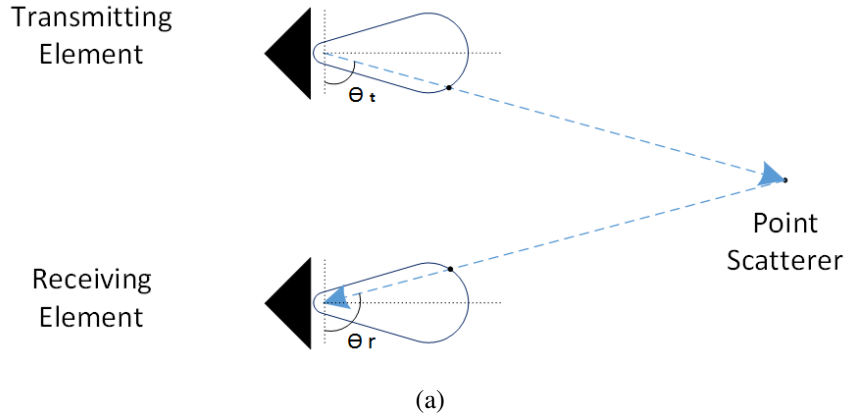
Figure 3.6: Angle between receive/transmit array element and target is illustrated

Previously, an element pattern simulation was provided for a Vivaldi antenna as in [27]. This element pattern is used for each transmit and receive elements in the MIMO topologies given in Fig. 3.2. Element pattern simulations were made with 1 GHz intervals in the operational bandwidth. But sampling frequency during the PSF calculations was 10 MHz, so an interpolation is needed. Nearest-neighbor interpolation is used since radiation pattern varies smoothly with frequency. The simulations of Vivaldi array element cover frequencies between 3 GHz to 10 GHz. Hence in the

analyses, 6.5 GHz center frequency and %100 bandwidth is chosen for simulations. The calculated PSF results are given in the following Fig.3.7,
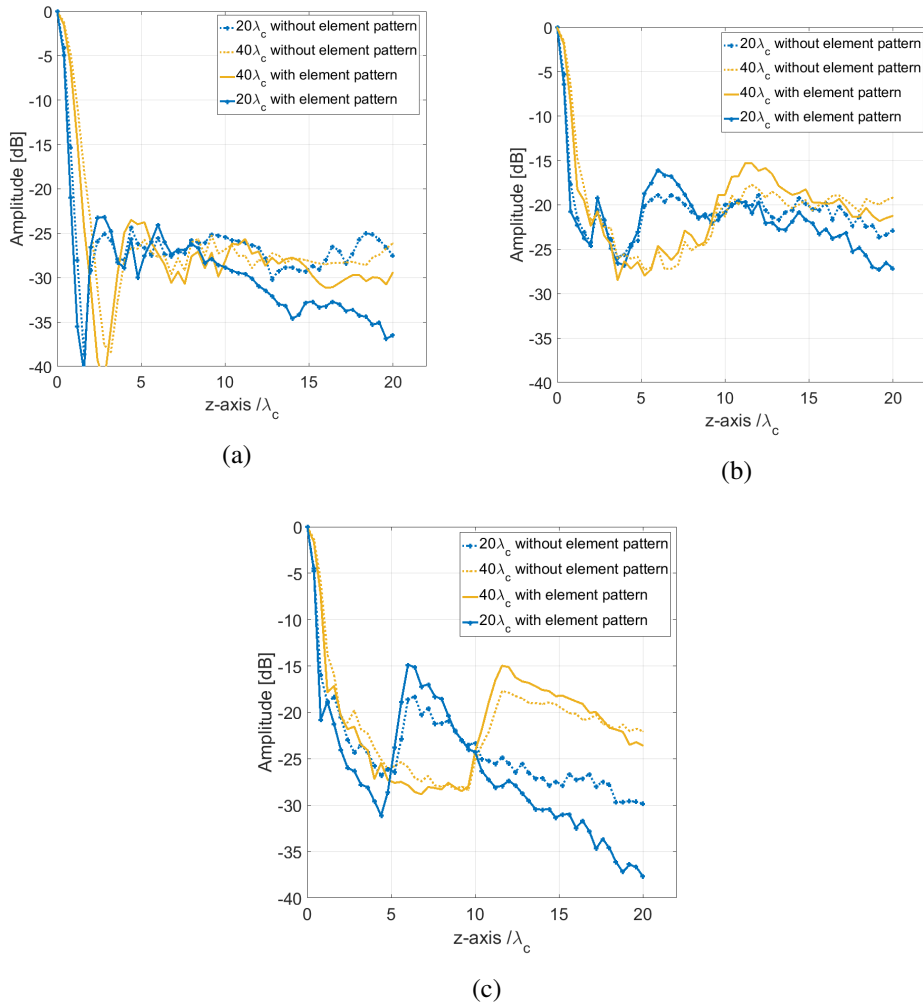

(a)

(b)

(c)

Figure 3.7: PSF calculated with and without element pattern for (a) curvilinear, (b) rectangular and (c) Mill's cross MIMO array configurations

In Fig.3.7 calculated PSF results are given for curvilinear, rectangular and Mill's cross MIMO array topologies with and without element pattern plotted on the same figure. In the simulation results first sidelobes are increased, especially for Mill's cross and rectangular type arrays. Whereas, side energy towards the end of the imaging space attenuates more. As a result sidelobe level close to the end of the imaging space is decreased with the incorporation of element pattern. For rectangular and Mill's cross MIMO array configurations, receiving and transmitting elements are not well distributed among eachother. Because of the element pattern, as the receive and transmit elements moving away from eachother the receiving elements start to receive highly

26

attenuated reflected signals from transmitting elements, so there will not be a virtual element for those far away receive-transmit pairs as shown in Fig.3.8. Hence, more empty locations in the virtual arrays and arrays behaves as if they are sparser. Consequently sidelobe levels increase.
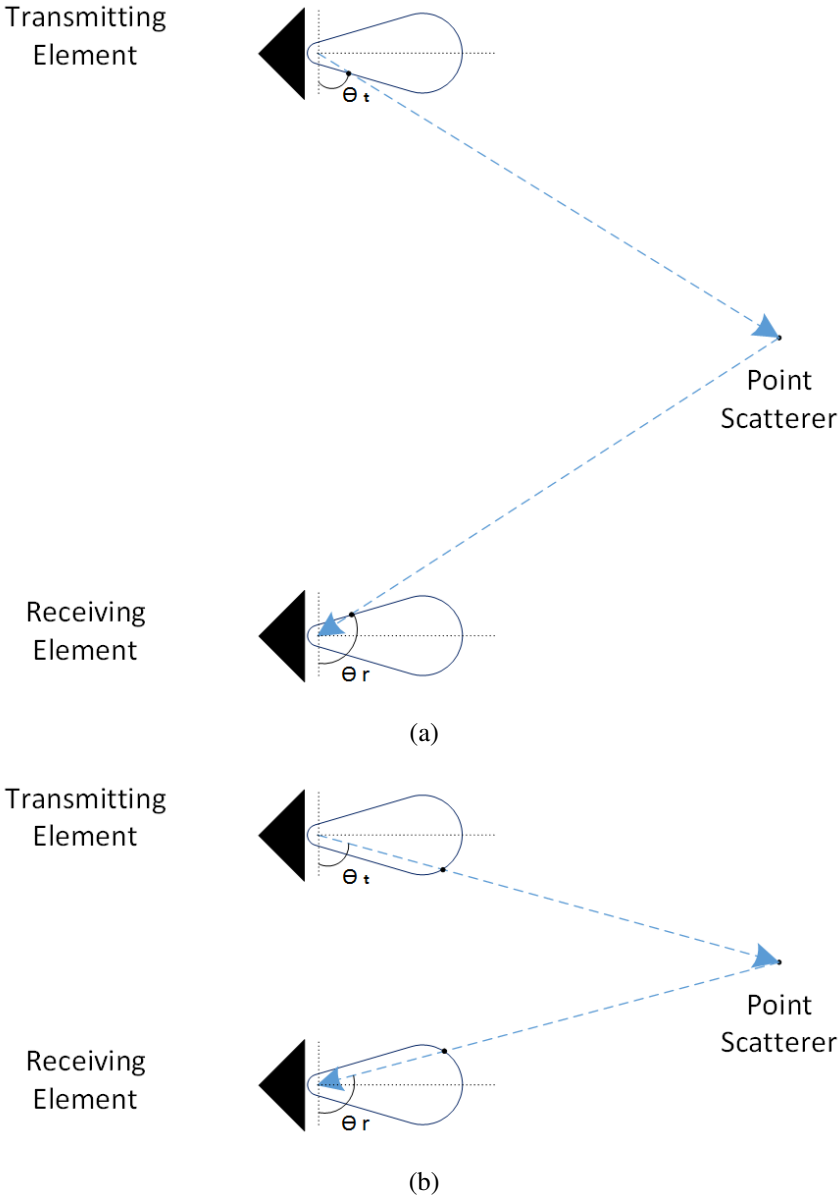

Figure 3.8: Illustration of effect of element pattern (a) for farther receive and transmit elements (b) for closer receive and transmit elements

In the comparisons given in Fig. 3.5, curvilinear MIMO array structure is best in terms of sidelobe levels and immunity to sidelobe degradation that occurs as range gets shorter. This makes it a good candidate for near-field imaging applications.

Therefore, the rest of the work will concentrate on curvilinear MIMO array structure.

In order to observe the effects of element pattern on multiple targets a simulation environment is set with 17 point scatterer. The targets are placed at a range of 0.5 m away from the antenna plane. Curvilinear MIMO array with 32 receive and 32 transmit elements is used in the analyses. Diameter of the antenna is 0.5m as in Fig. 3.9,
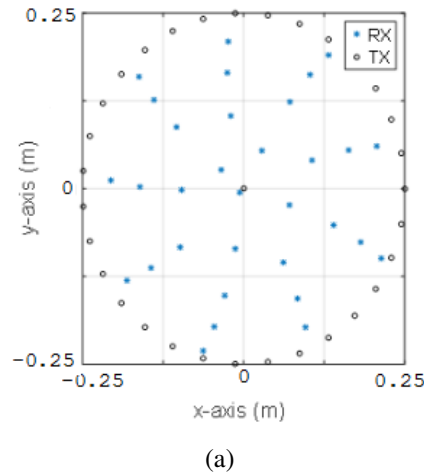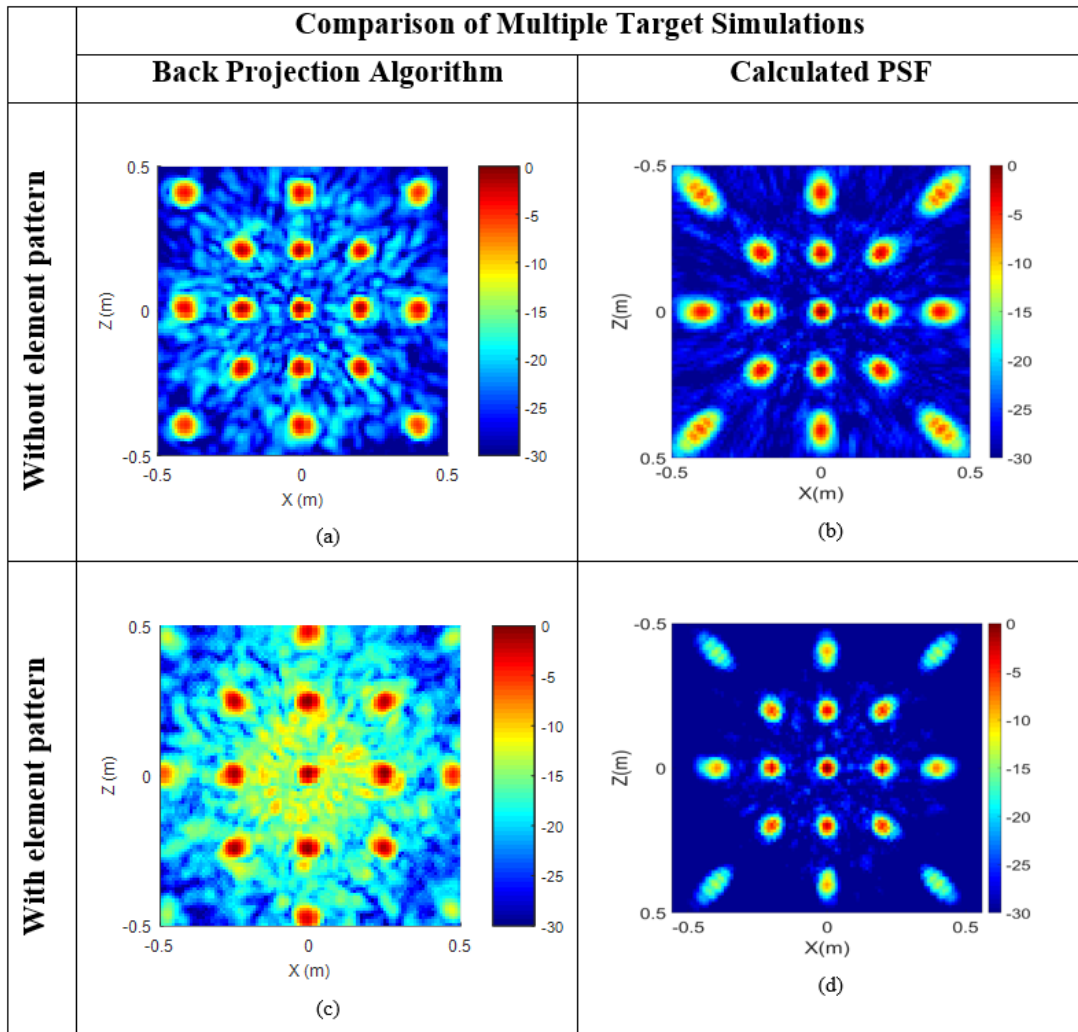

(a)

Figure 3.9: Curvilinear MIMO array for multiple target simulations.

In another work the same problem is studied by using Back Projection (BP) image reconstruction method. The measured signals that are the input data for the BP algorithm are generated by using two different approaches. First a simple spherical wave model is used to compute the signals received by the receiver antennas. Since isotropic elements are assumed, the result of this model are compared with the PSF obtained without element pattern. Then, the simulation results obtained from commercially available EM field simulator CST are used as the input for BP algorithm. Vivaldi antennas are used in CST simulations. Then BP results of this case are compared with the PSF obtained with element pattern.

When the reference work in Fig. 3.10(a). and Fig. 3.10(c). are compared with calculated PSF in Fig. 3.10(b). and Fig. 3.10(d)., it can be observed that element pattern increases the sidelobes. While the point targets at the corner of the imaging space can be clearly observed in Fig. 3.10a., they become invisible in Fig. 3.10(c) since the element patterns and mutual coupling between elements are considered in full-wave

28

| Comparison of Multiple Target Simulations | |
| Back Projection Algorithm | Calculated PSF |

Without element pattern — (a), (b)

With element pattern — (c), (d)

(a)

Figure 3.10: Comparison between PSF calculation method and calculations made with back projection and full-wave solvers in another study.Reference study (a) without element pattern, (c) with element pattern. Calculated PSF (b) without element pattern (d) with element pattern.

model. A similar trend is also observed from the PSF calculations in Fig.3.10(b). and Fig.3.10(d). Another important observation about the PSF results obtained in this work. As the target gets far away from the center of the array, the image of the target becomes elongated. This distortion in the image is attributed to the maximum projection method that considers the maximum value over all time instances.

3.4 Design of MIMO Array Topology for CWD

As a case study, an imaging system to be used in airport personnel security scanner for CWD is to be designed. In order to decide antenna topology, the final PSF calculation method which employs frequency domain pulse and includes element pattern is used. Generic systems mostly implements SAR type data acquisition as in [12–14], but SAR is a monostatic approach. Although, high resolution images can be obtained by SAR, required time for data acquisition is too long to be used in real time imaging applications that is vital for crowded places like airports. MIMO arrays significantly reduce data acquisition time. Therefore, using a single MIMO array or combining MIMO array structure with SAR (MIMO-SAR) might be a better alternative.

For this specific case 3 different topologies with curvilinear array structure will be investigated. The first one is a MIMO array consisting of 64 transmit and 64 receive elements with an array aperture of 2m x 2m. The other two structures will be MIMO-SAR examples. Two kind of movement can be done with the curvilinear array. It can be rotated around the center or can be moved to different locations in the array aperture. Equal number of measurement should be done for the comparison of the methods. Hence, as a second case, a 2m x 2m array but with 32 transmit and 32 receive elements is rotated 4 times with an angle of 90°. And finaly, as a last MIMO-SAR case a smaller subarray is used with 32 transmit and 32 receive elements and the array is moved both in horizontal and in vertical directions to cover the same aperture as the larger array (2m x 2m). Note that, all three configuration contains 4096 measurements. MIMO and MIMO-SAR array configurations given in Fig. 3.11,

PSF's are calculated for 6.5 GHz center frequency with a frequency domain pulse that has %100 bandwidth and element pattern simulation of a Vivaldi antenna operating in this frequency range are included in the analysis. A point target is assumed in analysis at a range of 0.5m away from the center of the array plane. The results can be seen in the Fig.3.12,

In Fig. 3.12, it is clear that MIMO array in Fig. 3.11a has the lowest sidelobes and MIMO-SAR array configuration obtained by 90° rotations can be classified as the second one. But, MIMO-SAR array configuration obtained by switching 4 different
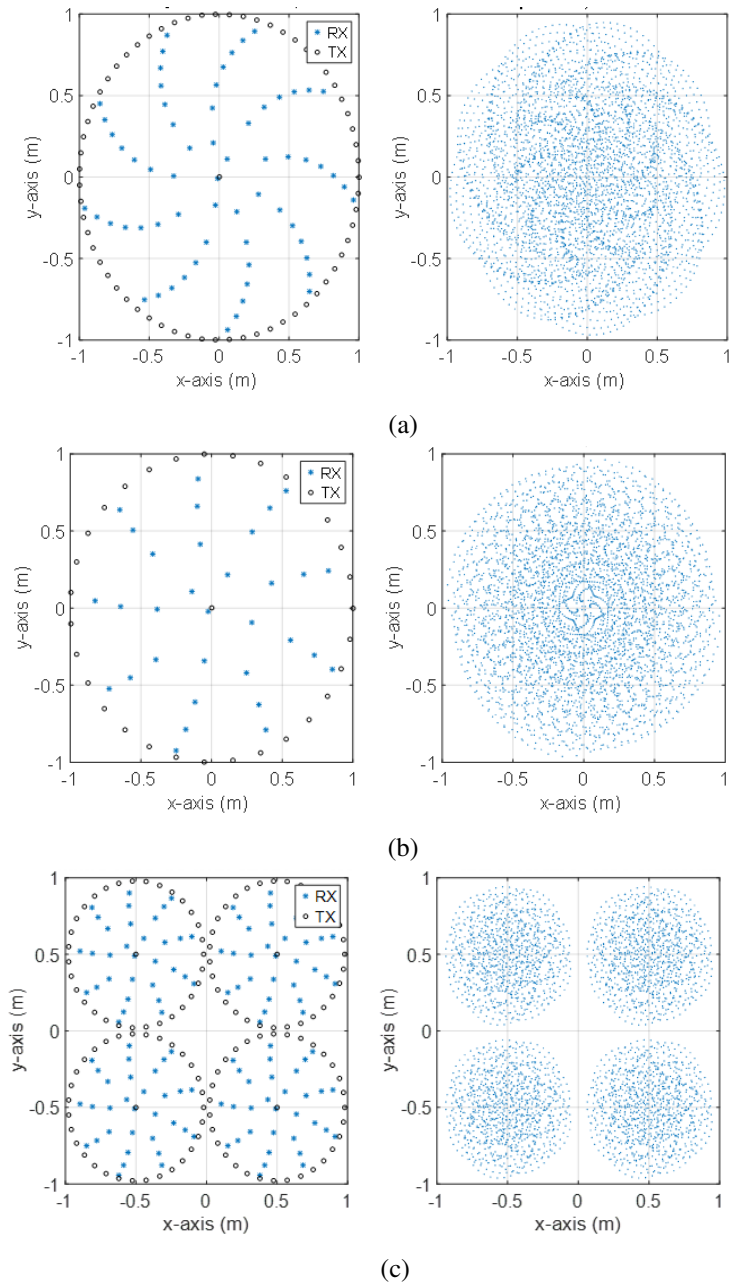
30

Figure 3.11: Different MIMO array structures (a) MIMO array with 64 transmit and 64 receive elements (b) 32 transmit and 32 receive elements with 90° rotations (rotated MIMO-SAR) (c)32 transmit and 32 receive elements with 4 different location over the aperture(shifted MIMO-SAR) and their virtual arrays on the right ,respectively.

location in Fig.3.11c has the highest sidelobe level especially at the angles close to the center. Also, beamwidth of this MIMO-SAR topology is clearly wider then the two. Empty locations in virtual array aperture of this topology may be the reason for this poor performance. To test the idea, the point target is moved to the corner of the
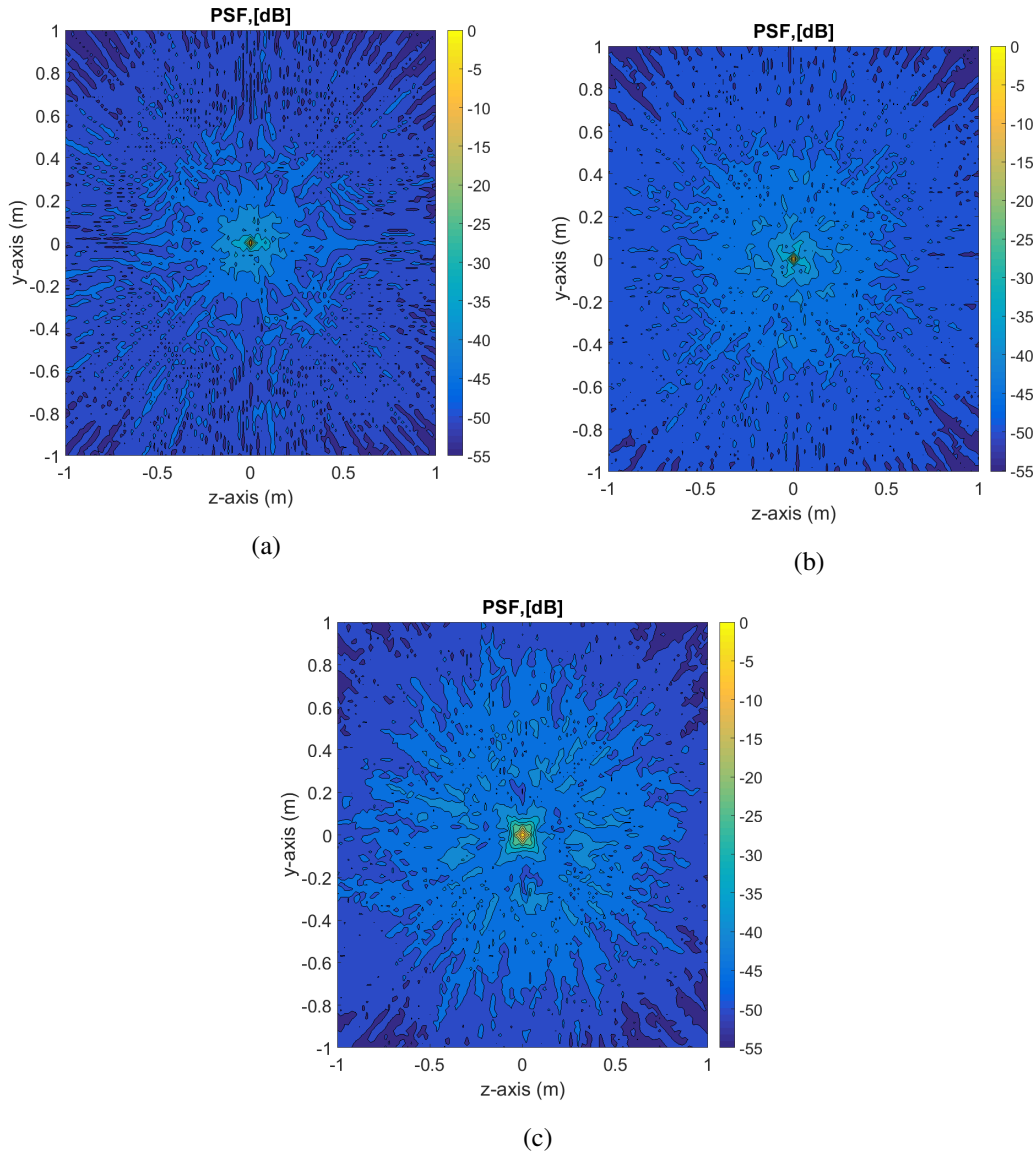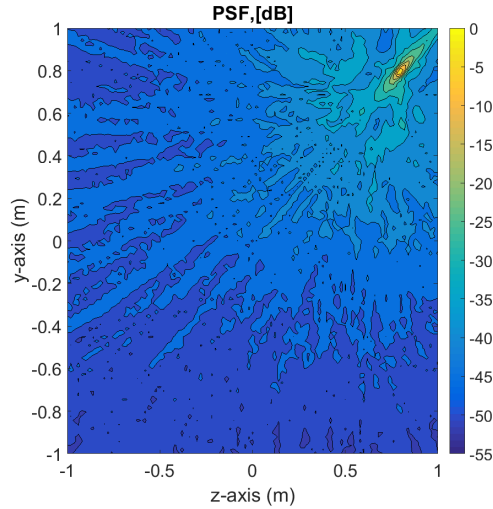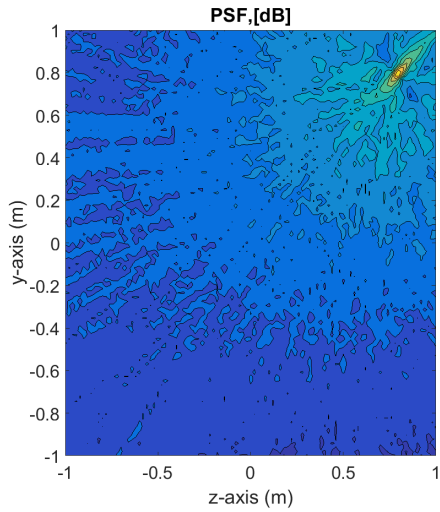
Figure 3.12: PSF of three different array topologies in Figure 3.11 point target (x,y,z)=(0.5m, 0, 0) (a)MIMO array,(b)rotated MIMO-SAR,(c)subarray MIMO-SAR

imaging space where MIMO array and rotated MIMO-SAR has no virtual element on the projection of point target to the array apertures. Then, simulations are repeated. The results of the off-axis point scatterer are given in Fig. 3.13.
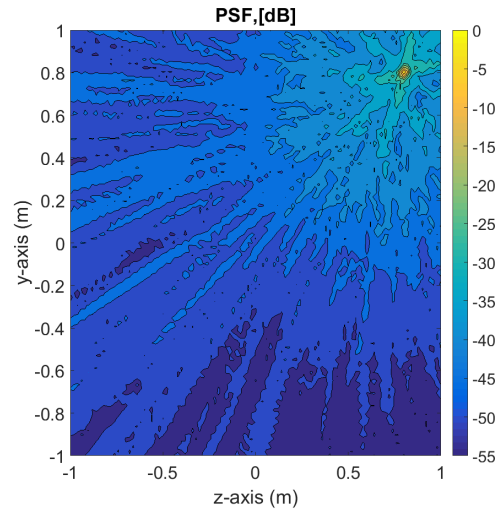
Suprisingly, subarray structure in Fig. 3.11c. gives the best result in terms of sidelobe level and beamwidth. So it is clear that, element density on projection of focal point on the virtual aperture is important for the performance. Hence, no empty regions must be left in the virtual aperture, if all regions of the imaging space to be observed.

(a)

(b)

(c)

Figure 3.13: PSF of three different array topologies in Figure 3.11 point target (x,y,z)=(0.5m, 0.8m, 0.8m)(a)MIMO array,(b)rotated MIMO-SAR,(c)subarray MIMO-SAR

Regarding the results in Fig. 3.12. and Fig.3.13., for a human body scan, array topology given in Fig. 3.14. can be prefered. In the proposed MIMO-SAR array topology a 32 transmitting and 32 receiving elements curvilinear subarray is moved end to end of the imaging space in 4 steps. The step size is arranged to obtain overlapping virtual arrays that cover most of the antenna aperture, as in Fig.3.14.

The simulation results for %100 bandwidth at center frequency 6.5 GHz are given in Fig3.15. Element pattern is taken into account. A point target 0.5 m away from
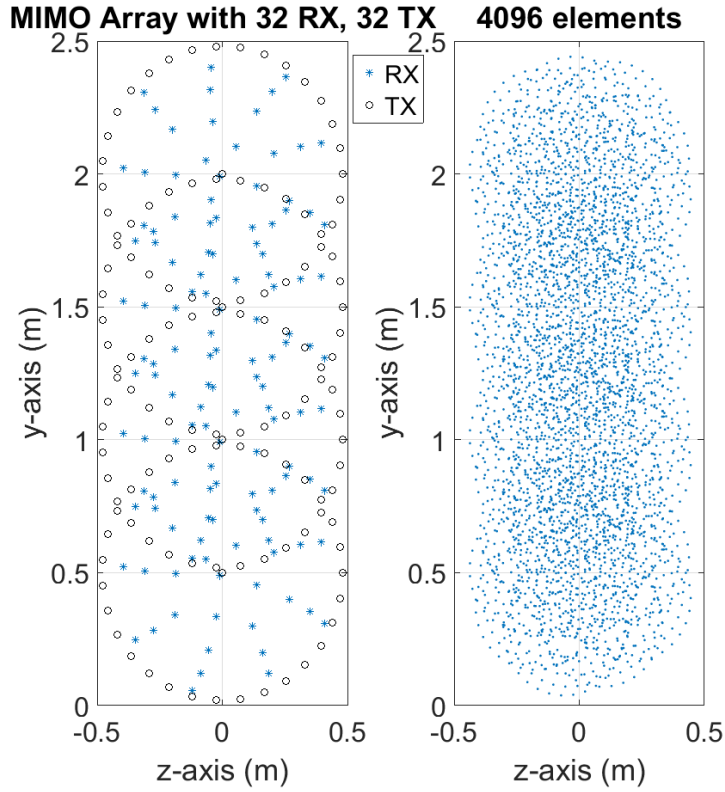
Figure 3.14: MIMO-SAR array structure to be used in human body scan.

the array plane is placed in the simulations. In order to see the performance of the proposed topology, point target is moved to several locations in the imaging space from the center to the corner point. Results are given in Fig. 3.15,

In Fig. 3.15(a). PSF is calculated for a point target at the center of the array axis. Then, in Fig. 3.15(b). and in Fig. 3.15(c). step by step point target is moved away from the center. Even at the corner of the imaging space the performance is good as seen in Fig. 3.15(c). It is clear from the results in Fig. 3.15 that proposed MIMO-SAR array topology provided equally well performance all over the imaging space. This is the result of overlapping virtual array that covers most of the array aperture. This MIMO-SAR array topology, can be an alternative for personnel screening systems.
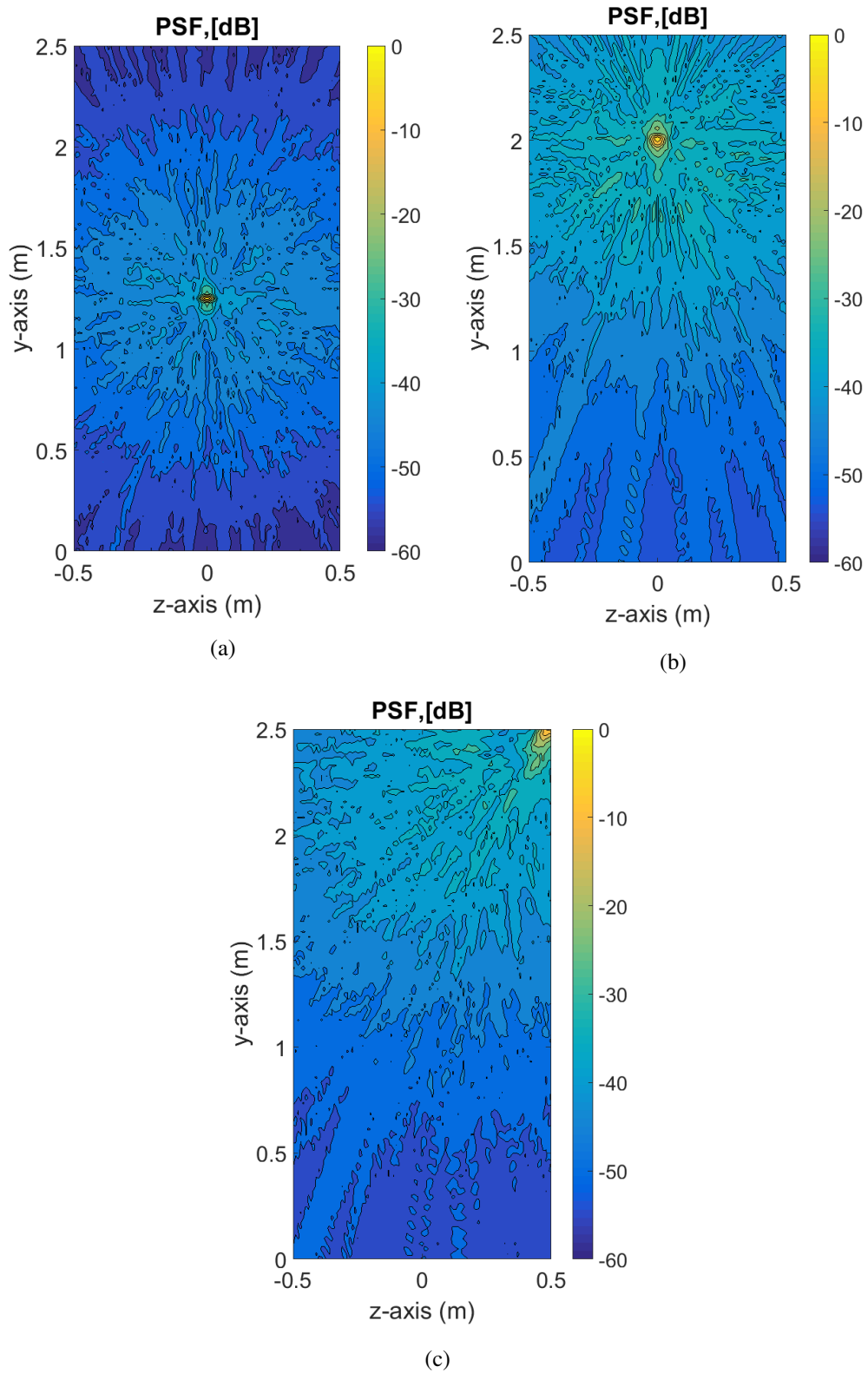
Figure 3.15: PSF of MIMO-SAR array topology given in Figure 3.14 (a) 2-D PSF at $x = 0, y = 0.5m$ (b) 1-D PSF maximum on different principal axis for $x = 0, y = 0.5m$ (c) 2-D PSF at $x = 0, y = 1m$ (d) 1-D PSF maximum on different principal axis for $x = 0, y = 1m$

CHAPTER 4

CONCLUSIONS

Today, imaging systems are widely spread in the several applications in our lives such as medical imaging, security, non-destructive testing and evaluation. In the most of applications Gamma Rays and X-Rays are employed, but they are harmful for organisms. Therefore they have limited usage on human body. So, microwave imaging systems can be an alternative. UWB MIMO arrays offer great advantages for short range microwave imaging applications. Real time operation for an imaging system to be used in vulnerable areas is urgent. Therefore, dense array structures should be avoided to prevent long computational time, effort and high production costs. In this thesis, it is aimed to develop an analysis tool for UWB MIMO arrays to be used in short range imaging applications. In this sense, thesis covers the following subjects.

Properties of UWB and NB arrays are investigated. In NB case, since NB signal has a long duration in time, radiated signals from the elements of the array interfere in each location in the visible space. But in UWB case; since UWB pulse is short in time, pulses radiated from the array elements interfere in a small region named as the interference region. Only in the interference region coherent energy build up occurs. Therefore, outside of this region, called as the non-interference region, sidelobes can not build up. By the existance of non-interference region in UWB arrays, naturally UWB arrays avoids sidelobe problem in NB array resultant from sparse array structures which is inevitable for real time imaging applications. Therefore by using UWB arrays, it is possible to design high resolution, low sidelobe arrays without using dense arrays. Furthermore, by using UWB arrays depth information can be resolved to construct 3-D volumetric images. Hence UWB technology is the most proper choice for imaging applications. Properties and theories related to UWB arrays are revisited

which form a basis for sparse UWB array design.

Further reduction of data acquisition time can be provided by employing MIMO arrays. Therefore, an analysis tool based on point spread function for UWB MIMO arrays is proposed. UWB array analysis should be made in time domain rather than conventional frequency domain analysis applied on NB arrays. If closer approximation to the practical case is needed, this method provide element pattern of the antenna elements to be taken into account in frequency domain.

When the method is applied on generic MIMO imaging array topologies in the literature, without the need for advanced image reconstraction algorithms and numerical solvers close results to the experimental works is reached. Advantages of MIMO and MIMO-SAR methods on SAR imaging method is discussed. Finally, an array structure for UWB near-field MIMO imaging applications that is proper for personnel screening systems to be used in airports is proposed.

REFERENCES

[1] X. Zhuge, "Short-range ultra-wideband imaging with multiple-input multiple-output arrays," Ph.D. dissertation, Delft University of Technology, 2010.

[2] M. Wernick and J. Aarsvold, *Emission tomography. The fundamentals of PET and SPECT*. California, USA: Elsevier Academic Press, 2004.

[3] U. Customs and B. Protection. CSI: Container Security Initiative. [Online]. Available: https://www.cbp.gov/border-security/ports-entry/cargo-security/csi/csi-brief

[4] A. Moffett, "Array factors with non uniform spacing parameters," *IRE Trans. Anetennas Propagat.*, vol. AP-10, pp. 131–146, 1962.

[5] N. G. Skolnik, M.I. and J. W. Sherman, "Dynamic programming applied to unequally spaced arrays," *IEEE Trans. Antennas Propag.*, vol. AP-12, pp. 35–43, 1964.

[6] A. Ishimaru and Y. Chen, "Thinning and broadbanding antenna arrays by unequal spacings," *IEEE Trans. Antennas Propag.*, vol. AP-13, pp. 34–42, 1965.

[7] Y. Lo and S. Lee, "A study of space tapered arrays," *IEEE Trans. Antennas Propag.*, vol. AP-14, pp. 22–30, 1966.

[8] B. Steinberg, *Principles of Aperture and Array Systems Design*. New York, USA: Wiley, 1976.

[9] J. L. Schwartz, "Ultrasparse,ultrawideband arrays," Ph.D. dissertation, University of Pennsylvania, 1996.

[10] G. R.Lockwood, P.-C. Li, M. O'Donnell, and F. S. Foster, "Optimizing the radiation pattern of sparse periodic linear arrays," *IEEE Trans. on Ultrasonics, ferroelectrics and Frequency Control*, vol. 43, pp. 7–14, 1996.

[11] G. Lockwood and F. Foster, "Optimizing the radiation pattern of sparse periodic two-dimensional arrays," *IEEE Trans. on Ultrasonics, ferroelectrics and Frequency Control*, vol. 43, pp. 15–19, 1996.

[12] A. T. S. Yarovoy, P. Aubry, P. Lys, and L. Ligthart, "UWB Array-Based Sensor for Near-Field Imaging," *IEEE Trans. Microw. Theory Tech.*, vol. 55, pp. 1288–1295, 2007.

[13] J. McFee, V. Aitken, R.Chesney, Y.Das, and K. Russell, "Multisensor vehicle-mounted teleoperated mine detector with data fusion," in *in Proc. SPIE Detection and Remediation Technologies for Mines and Minelike Targets*. IEEE, 1998, pp. 1082–1093.

[14] R. Cosgrove, P. Milanfar, and J.Kositsky., "Trained detection of buried mines in SAR images via deflection-optimal criterion," *IEEE Trans. Geosci. Sens.*, vol. 42, pp. 2569–2575, 2004.

[15] X. Zhuge and A. G. Yarovoy, "A Sparse Aperture MIMO-SAR-Based UWB Imaging System for Concealed Weapon Detection," *IEEE Transactions on Geoscience and Remote Sensing*, vol. 49, no. 1, pp. 509–518, Jan 2011.

[16] B. T. Cetin and L. Alatan, "Performance comparison of different sparse array configurations for ultra-wideband, near-field imaging applications," in *11th European Conference on Antennas and Propagation (EUCAP)*. IEEE, 2017, pp. 458–460.

[17] D.Lamensdorf and L.Susman, "Baseband-pulse-antenna techniques," *IEEE Trans. Electromag.Mag.*, vol. 36, pp. 20–30, 1994.

[18] G. Quintero, J.F.Zurcher, and A. Skrivervik, "System fidelity factor: a new method for comparing UWB antennas," *IEEE Trans. Antennas Propag.*, vol. 59, pp. 2502–2512, 2011.

[19] C. Liao, P.Hsu, and D.C.Chang, "Energy patterns of UWB antenna arrays with scan capability," *IEEE Trans. Antennas Propag.*, vol. 59, pp. 1140–1147, 2011.

[20] J. McLean, H.Foltz, and R.Sutton, "Pattern descriptors for UWB antennas," *IEEE Trans. Antennas Propag.*, vol. 53, pp. 553–559, 2005.

[21] F. Lockwood, G.R.and Foster, "Optimizing sparse two-dimensional transducer arrays using an effective aperture approach," in *IEEE Ultrasonic Symposium Proceedings*. IEEE, 1994, pp. 1497–1501.

[22] B. Steinberg and H. Subbaram, *Microwave Imaging Techniques*. New York, USA: Wiley, 1991.

[23] X.Zhuge, A. Yarovoy, T. Savelyev, and L. Ligthart, "Modified Kirchhoff migration for UWB MIMO array-based radar imaging," *IEEE Trans. Geosci. Remote Sens.*, vol. 48, pp. 2692–2703, 2010.

[24] J. Lopez-Sanchez and J. Fortuny-Guasch, "3-D radar imaging using range migration techniques," *IEEE Trans. Antennas Propag.*, vol. 48, pp. 728–737, 2000.

[25] J. Aliferis, T. Savelyev, M. J. Yedlin, J. Y. Dauvignac, A. Yarovoy, C. Pichot, and L. Ligthart, "Comparison of the diffraction stack and time-reversal imaging algorithms applied to short-range UWB scattering data," in *2007 IEEE International Conference on Ultra-Wideband*, Sept 2007, pp. 618–621.

[26] X. Zhuge and G. A. Yarovoy, "Study on two-dimensional sparse MIMO UWB arrays for high resolution near-field imaging," *IEEE Trans. on Antennas Propag.*, vol. 60, pp. 4173–4181, 2012.

[27] Y. Ma, F. Zhu, Z. Abidin, S. Pang, F.Li, R. Abd-Alhameed, C. See, J. Fan, L. Liu, X. Chai, C. Jin, and B. Pen, "Vivaldi Antenna with balun feed for SKA feeding system in UWB," in *URSI AT-RASC 2015 Conference*. IEEE, 2015, pp. 4–pp.